RSC Advances

REVIEW

View Article Online
View Journal | View Issue

Cite this: *RSC Adv.*, 2025, **15**, 24510

Review on the synergistic effect of adsorption and photocatalytic degradation of patulin by functionalized graphitic carbon nitride nanomaterials and hydrogels

Meie Zheng,‡ Wenwen Li,‡ Fei Ma, * Yujia Shao, Mengru Guo, Xinyue Gao and Junbo Du

The efficient removal of patulin (PAT) contamination in food is an important challenge in the field of food safety, and the traditional single adsorption or photocatalytic techniques have bottlenecks such as low efficiency and difficult regeneration. The integration of adsorption–photocatalytic degradation by utilizing the synergistic effect of functionalized graphite-phase carbon nitride (g-C_3N_4) nanomaterials and hydrogels has proved to be a highly promising solution. However, how to construct a bifunctional material system with both high adsorption capacity and long-lasting photocatalytic activity is still a current research challenge. In this paper, we systematically review the recent progress of g-C_3N_4-based nanocomposites and hydrogel materials and their recent advances for enhancing the removal efficiency of PAT. This review provides a theoretical basis and technical reference for the development of "adsorption–degradation" smart material systems.

Received 14th February 2025
Accepted 22nd June 2025

DOI: 10.1039/d5ra01082a

rsc.li/rsc-advances

1 Introduction

In 1943, Harold Raistrick isolated PTA for the first time from *P. gray-yellowiasis*. After identification, the British Medical Research Center conducted a study on PAT, which then used PAT as an antibacterial agent for some specific bacteria with either Gram-positive or Gram-negative characteristics. Although, in 1944, the research center staff discovered its toxic effects.[1] PAT has been detected in numerous foods. It is prevalent in fruits, vegetables, and their respective products. Among them, apples and apple-based products are particularly notable sources,[2] and it is employed as a quality benchmark for the apples used in juice-making or compost-making.[3] Research findings indicate that the extent of PAT accumulation primarily hinges on the specific strain. In contrast, it has relatively little connection with the various storage stages that apples go through during extended storage periods.[4] Therefore, the key to preventing and controlling PAT in food is to control strains that can produce PAT toxins. To achieve this goal, a series of control measures can be taken, including preharvest control (such as selecting resistant varieties and implementing pest management), control during harvest (such as timely and manual harvesting) and postharvest control measures (such as high-pressure cleaning and cold chain storage), to maximize the prevention of contamination of food by strains carrying PAT toxins.[5] However, since contamination may take place at each and every link within the food supply chain it is not possible to ensure that there is no strain or zero PAT in the food chain that produces PAT toxins. Furthermore, PAT possesses notable physical and chemical steadiness. Due to this characteristic, its structure is not easily damaged during the food processing stage. Moreover, PAT can build up through the food chain, exerting considerable influences on the health of mammals. These impacts involve symptoms such as headaches, nausea, pulmonary edema, injuries to the liver and kidneys, along with neurotoxicity and immunotoxicity. PAT can trigger a variety of acute and chronic diseases and complex responses at the cellular level and has been listed as the third category of suspected carcinogen by the International Cancer Research Institute.[6–9] In this context, the World Health Organization (WHO, 2005), the U.S. Food and Drug Administration (FDA) and the European Union (EU) consistently stipulate that the maximum acceptable content of PAT in apple juice is 50 μg L^{-1} and that in children and babies. The PAT content was limited to 10 μg L^{-1}.[10] Therefore, putting into practice powerful and effective detoxification strategies to regulate PAT tainting in fruits and their derivatives is of great significance. In recent times, a variety of techniques have been employed for the elimination of mycotoxins (Fig. 1). These encompass ionizing radiation methods like gamma-ray irradiation and electron-

Hubei Key Laboratory of Resource Utilization and Quality Control of Characteristic Crops, College of Life Science and Technology, Hubei Provincial Engineering Research Center of Key Technologies in Modern Paper and Hygiene Products Manufacturing, School of Mechanical Engineering, Hubei Engineering University, Xiaogan, Hubei Province, 432000, P. R. China. E-mail: 376144258@qq.com

‡ These authors contributed equally to the work and are co-first authors.

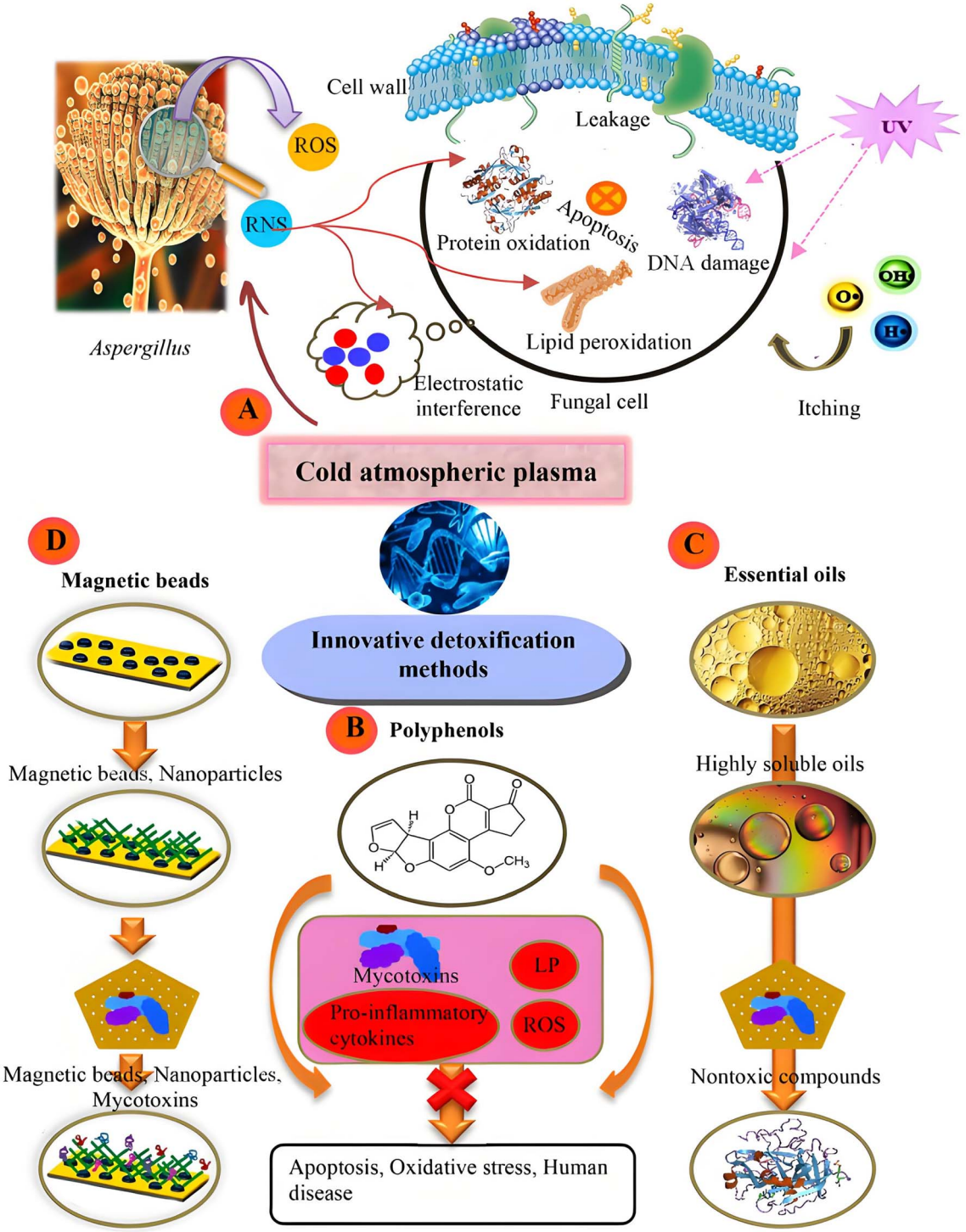

Fig. 1 Methods for controlling mycotoxin contamination. (A) Cold atmospheric plasma method, (B) polyphenols, (C) natural essential oils, and (D) magnetic materials and nanoparticles.[14]

beam bombardment, optical techniques such as ultraviolet illumination and pulsed-light emission, aqueous-based treatments represented by electrolytic water application, plasma-related technologies typified by cold-plasma utilization, and degradation processes based on catalysis, with photocatalytic degradation being a prime example,[11–13] where photocatalytic degradation occurs because of the recovery rate of mycotoxins. The characteristics of simplicity, greenness, and high efficiency have attracted widespread attention.

The abnormal stability of PAT under acidic environment and heat treatment leads to the difficulty of effective degradation by conventional means, while the physical adsorption method is

limited by the bottleneck of poor selectivity and high regeneration cost. The traditional g-C_3N_4 materials still face the core challenges of high photogenerated carrier complexity, limited specific surface area, and insufficient adsorption selectivity in complex food matrices, which seriously limit their practical application efficacy. Recent studies have shown that the carrier separation efficiency can be significantly improved (by 3–5 times) through interfacial engineering strategies, such as heterostructure construction and elemental doping; the combination of 3D hydrogel network and molecular imprinting technology optimises the material's adsorption capacity (>200 mg g^{-1}) and photocatalytic active site accessibility, resulting in a PAT degradation rate of more than 90%. Nevertheless, the analysis of the conformational relationship of the materials is mostly limited to a single performance index, and there is still a lack of systematic understanding of the key scientific issues such as the mechanism of adsorption–photocatalysis synergy, the interference effect of food components, and the cyclic stability of the materials.

In this review, we present a comprehensive overview of the recent progress of functionalized g-C_3N_4-based materials for PAT removal, focusing on: (1) the regulation of adsorption–photocatalytic synergistic performance by multidimensional nanostructural design; (2) the influence of coexisting components such as polysaccharides and pigments on the degradation pathway of food matrices; and (3) regeneration strategies and life-cycle assessment of the materials for large-scale applications. By clarifying the current technological bottlenecks and theoretical gaps in knowledge, we will provide prospective guidance for the development of new photocatalytic materials that are highly efficient, stable and food-compatible.

2 Overview of graphite-phase carbon nitride

2.1 Structure of graphite-phase carbon nitride

g-C_3N_4 is a 2D nanomaterial using a stratified graphite formation. Its basic structural units are stacked with atomic layers formed linked by the covalent bonds between C atoms and N atoms, within which tri-*s*-triazine represents the most stable unit (Fig. 2A). The topological structure of g-C_3N_4 is a 2D graphitic structure connected by a tertiary amine. The built-in functional groups include –NH_2/–NH–/=N–, which provide many surface defects and reactive sites for g-C_3N_4. The five varieties of graphite-phase carbon nitride structures encompass α-C_3N_4, β-C_3N_4, g-C_3N_4, cubic-C_3N_4 and pseudocubic-C_3N_4. Among them, g-C_3N_4 has the lowest binding energy, the lowest hardness and the most stable structure.[15,16]

The C atoms and N atoms in g-C_3N_4 possess lone pairs of electrons within the p_z orbital. These electrons can interact with each other, resulting in the formation of a large π bond that bears resemblance to the benzene ring. Moreover, through sp^2 hybridization, a highly delocalized conjugated system is established. This conjugated system endows graphite-phase carbon nitride with a unique energy band structure, it is divided into three parts: a bonding band, a free-electron band and a band gap. The energy separation between the bonding band and the free-electron band amounts to 1.9 eV, while the width of the band gap is 0.4 eV. The interlayer distance of g-C_3N_4 is approximately 0.345 nm, which has a value that is slightly greater than the layer spacing of graphene (0.34 nm) and has better photoelectric and mechanical properties. In addition, g-C_3N_4 has a 2D structure, therefore, an appropriate external force can be applied to overcome the intermolecular van der Waals force between layers. Subsequently, by carefully peeling off the bulk g-C_3N_4, a 2D g-C_3N_4 nanosheet that has a significantly large specific surface can be successfully obtained. These nanosheets are rich in active sites and have excellent photoelectric properties, which are conducive to the progress of photocatalytic reactions (Fig. 2B). At present, scientific researchers have obtained g-C_3N_4 nanosheets through different methods, including top-down peeling of blocked g-C_3N_4 and assembling the precursor from bottom to top in a 2D manner. These two preparation methods can be further subdivided into ultrasonic-assisted liquid peeling,[19] acid etching,[20] thermal oxidation peeling,[21] *etc.*, in order to synthesize g-C_3N_4 nanosheets with low cost, simplicity and rapidity. Among them, the thermal oxidation peeling method is low in cost and environmentally friendly and is considered to be an effective method for obtaining g-C_3N_4 nanoscale sheets.[22] Furthermore,

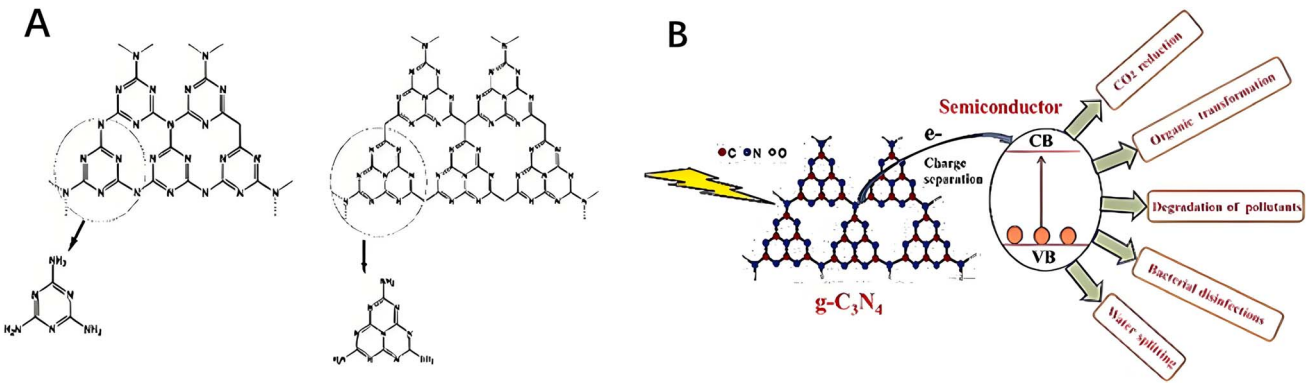

Fig. 2 Photocatalytic reactions of carbon–nitride-based materials. (A) g-C_3N_4 has two structures, namely the triazine (a) and the tri-*s*-triazine.[17] (B) Mechanism and application of g-C_3N_4 photocatalytic reaction.[18]

adjusting the synthesis parameters allows for the production of g-C_3N_4 photocatalysts that exhibit varying sizes and shapes, ranging from 0D quantum dots, 1D nanotubes, 2D nanoscale sheets, and 3D porous frameworks, as well as diverse nanoscale dimensions. The material exhibits excellent electron transfer properties, stable optical properties, porosity, and distinctive structural characteristics marked by a significant specific surface area that endow it with substantial potential for utilization in the area of photocatalytic degradation.[16]

2.2 The properties inherent in graphite-phase carbon nitride

g-C_3N_4 has a variety of excellent physical and chemical properties, such as electrochemical properties, thermal stability, chemical stability and catalytic activity. These properties give g-C_3N_4 broad application prospects in ambient photocatalytic degradation, energy conversion, electrochemical energy conversion and storage (Fig. 3).

First, g-C_3N_4 has high conductivity and electron mobility, which results in good electrochemical activity. Through doping and surface modification, its electrical properties can be controlled, expanding its applicability in devices based on electronics, sensors, and various other domain. Second, g-C_3N_4 has good thermal stability and can exist stably below 600 °C, and its structure and mass do not change significantly. When the temperature increases above 600 °C, g-CNQDs gradually decompose; at 750 °C, g-C_3N_4 completely decomposes. Furthermore, g-C_3N_4 has good chemical stability and strong corrosion resistance to chemical substances such as acids, alkalis, oxidants and reducing agents. It can remain stable in air, water, acid and alkali. After that, g-C_3N_4 possesses superior adsorption capabilities, making it suitable for adsorbing and purifying gases, pollutants, and other substances. Its edges are rich in basic groups, such as –NH and –NH_2, which can provide rich binding sites and achieve the adsorption and elimination of acidity pollutants through electrostatic attraction. Furthermore, the conjugated π region in its plane can adsorb aromatic pollutants by means of π–π conjugation.

Finally, g-C_3N_4 has high catalytic activity and can be used in catalytic reactions, environmental purification and other fields. With its role as an effective photocatalyst, it finds wide-spread uses in the domains of splitting water *via* photocatalysis and reducing carbon dioxide through photocatalysis. In 1924, Baur and Ferret reported through an experiment that silver salt can be reduced to metallic silver under the action of ZnO. This discovery first proposed the concept of photocatalysis.[24] Since Fujishima and Honda made groundbreaking research results in 1972, researchers have developed a strong interest in photocatalytic technology.[25] On the one hand, researchers are working hard to develop efficient semiconductor photocatalysts to enhance the efficiency of photocatalytic reactions. On the other hand, we are also constantly expanding the application of photocatalytic technology, from initial water cracking to all aspects of life, such as medical care, environmental governance, and agricultural production. In terms of pollutant removal, in 1976, Carey *et al.* used TiO_2 to photocatalyze the removal of PCBs under ultraviolet light, which has since inspired much related research.[26] At present, photocatalytic technology has also made certain progress in the process of catalytically oxidizing a wide range of organic contaminants, for instance colorants, pesticides, antibiotics, and mycotoxins. The core mechanism behind semiconductor photocatalytic reactions involves the effective conversion of solar energy into electrical or chemical energy, and this is of vital importance for diverse applications within energy-related domains. In this process, semiconductor catalysts play a key role, but they themselves remain unchanged before and after the reaction. When a semiconductor photocatalyst absorbs light energy equal to or exceeding its band-gap energy, electrons in the valence band (VB) become energized and transition to the conduction band (CB). Meanwhile, holes are left behind in the VB. Afterward, the

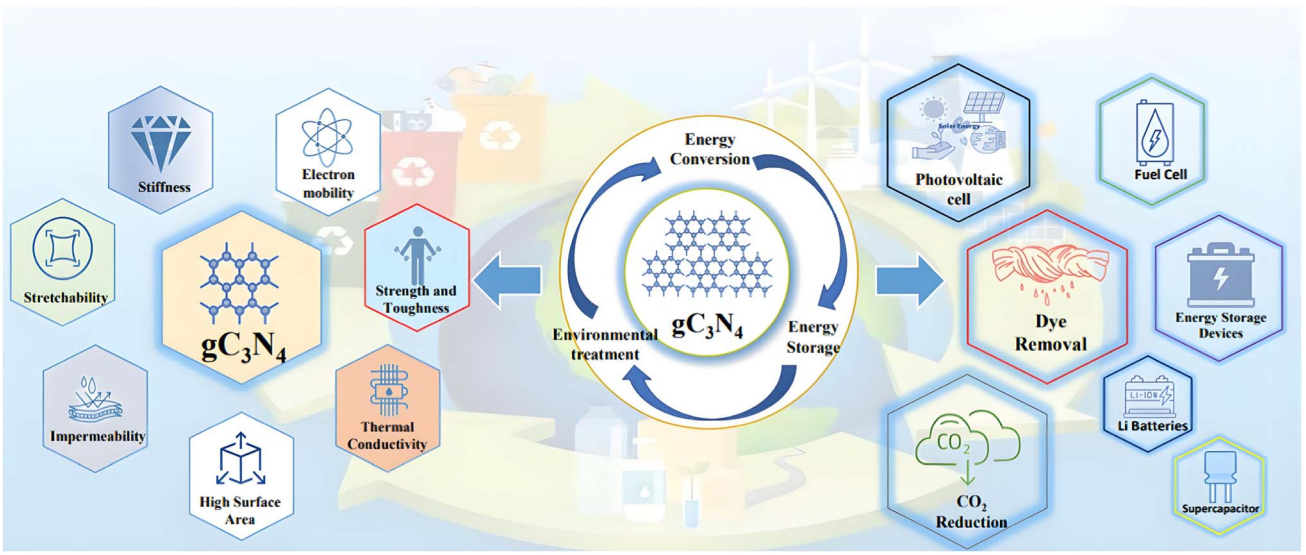

Fig. 3 Multifaceted applications and properties of g-C_3N_4.[23]

energized electrons and the corresponding holes travel to the surface of the material, initiating redox reactions in the presence of species adsorbed on the surface of the catalyst.[27] In the aqueous-phase reaction system, photogenerated electrons also undergo a free radical chain reaction with solvent molecules. This process generates a variety of reactive oxygen species. This includes, among others, hydroxyl radicals ($\cdot OH$), superoxide anion radicals ($\cdot O^{2-}$), and singlet oxygen (O^{2-}), but is not restricted to these species. Owing to their strong oxidative properties, these reactive oxygen species can further participate in the oxidation process on outer layer, thereby enhancing the effect of the photocatalytic conversion.[28]

2.2.1 The adsorption characteristics of graphite phase carbon nitride. The coupling application of adsorption and photocatalysis can effectively promote the complete degradation of dyes in a short period of time, and also help extend the service life of the material.[29] However, many photocatalysts currently perform poorly in terms of the amount of dye adsorbed, and the effects of photogenerating electrons, holes and some reactive oxygen species are limited. In recent years, 2D nanomaterials have garnered significant attention. This is due to the fact that they possess numerous advantages and satisfy most of the conditions necessary for excellent adsorbents. Its significant features include a large specific exposed surface and abundant reactive points, among which g-C_3N_4 stands out notably. g-C_3N_4 nanosheets are rich in basic groups such as –NH and –NH_2, which can provide rich binding sites and achieve the adsorption and removal of acidic pollutants *via* electrostatic binding.[30] Furthermore, the conjugated π region in the g-C_3N_4 plane can adsorb aromatic pollutants by means of π–π conjugation. Based on the aforementioned characteristics, g-C_3N_4 can act as an adsorbent and photocatalyst with excellent performance in removing pollutants in wastewater.[31,32]

Research by Wang *et al.* demonstrates that the particle size of g-C_3N_4 exerts a profound influence on its adsorption capacity and overall catalytic efficiency.[33] Specifically, reducing the particle size of g-C_3N_4 significantly enhances its specific surface area, thereby exposing a greater density of active sites on the material surface. This augmentation elevates the probability of pollutant encounter and adsorption by amplifying the accessible interface between the catalyst and environmental contaminants. The expanded specific surface area not only accelerates pollutant sequestration but also provides abundant reactive interfaces for subsequent catalytic reactions.

However, particle size reduction, while increasing the specific surface area, may concurrently compromise the in-plane piezoelectric polarization strength of g-C_3N_4, thereby undermining its piezocatalytic performance. Piezoelectric polarization is a critical determinant in piezocatalysis, governing the segregation and migration of charge carriers across the material surface to facilitate the generation of reactive oxygen species (ROS). These ROS serve as pivotal mediators for pollutant degradation. Consequently, the rational design of g-C_3N_4-based catalysts necessitates meticulous particle size optimization to reconcile surface area expansion (for enhanced adsorption) with the preservation of adequate piezoelectric polarization. This integrated optimization framework offers a novel strategy for developing high-efficiency, eco-friendly g-C_3N_4 catalysts. Beyond environmental remediation, such advancements hold transformative potential for clean energy technologies and related interdisciplinary applications, underscoring their strategic value in sustainable innovation.

Wang and colleagues conducted a systematic research into the adsorption behavior of g-C_3N_4 prepared from different precursors and explained the formation mechanism, influencing factors and relative contributions of various interactions in the surface adsorption process of humus on g-C_3N_4. Due to the combined influence of the amino group of g-C_3N_4 and the heptazine ring, along with the aromatic rings and oxygen-containing functional groups within humus, the adsorption process of humus on g-C_3N_4 is caused mainly through electrostatic attractions, π–π stacking, and hydrogen bonding interaction.[34] Cai and colleagues further confirmed that g-C_3N_4 nanosheets, as adsorbents with excellent performance, have unique adsorption properties. For example, Cd^{2+} can achieve an adsorption capacity of 94.40 mg g^{-1} by coordinating with C and N atoms within the triazine ring unit of g-C_3N_4. At pH = 7.0, the capacity of MB adsorption by g-C_3N_4 can reach 42.19 mg g^{-1} owing to π–π conjugation interactions and electrostatic gravity. Moreover, the composite materials of g-C_3N_4 also demonstrate favorable adsorption capabilities. For instance, Guo and his/her team managed to synthesize a g-C_3N_4/MnO_2 composite abundant in active sites through an *in situ* deposition approach. The maximum adsorption of Pb(II) in water by this composite material is as high as 204.10 mg g^{-1}. This result fully demonstrates that g-C_3N_4. As an adsorbent, it has broad application prospects.[35]

2.2.2 Photocatalytic properties of graphite phase carbon nitride. As a nonmetallic n-type semiconductor polymer, g-C_3N_4 has unique electrical, optical, thermodynamic and chemical properties. It is nontoxic, simple to prepare, stable in structure, can also be passed through the control synthesis method for regulating the shape and dimensions of g-C_3N_4, and it can be easily recombined with other semiconductors, making g-C_3N_4 a type of photocatalytic material with great application prospects.[36] It was in 2009 that Wang and his colleagues first discovered that g-C_3N_4 can photocatalyze the decomposition of water, producing H_2 and O_2. Since then, g-C_3N_4 nanophotocatalysts have become ideal candidate materials holding significant promise in the domains of energy utilization and environmental restoration because of their distinctive characteristics and have found extensive application in the photocatalytic decomposition of water and the breakdown of organic contaminants in water.[18]

g-C_3N_4 possesses a band gap of roughly 2.70 eV, enabling it to react to visible light.[37] Furthermore, the preparation process of g-C_3N_4 is relatively simple. Through a heat condensation reaction, g-C_3N_4 can be prepared using several low-cost and nitrogen-rich precursors as raw materials. At present, urea and melamine are the two most commonly used precursors. In addition, thiourea and dicyanide can likewise be employed in the synthesis of g-C_3N_4.[38] Apart from the heat condensation technique, g-C_3N_4 can also be synthesized through the processes of self-assembly of molecules,[39] heating synthesis

Table 1 Comparative study of g-C_3N_4-based composite materials

Materials	Findings	Advantage	Disadvantage	Ref.
g-C_3N_4/TiO_2	It has a good degradation effect on antibiotics such as tetracycline in water; it has shown certain potential in photocatalytic water splitting to produce hydrogen	The addition of TiO_2 broadened the photoresponse range of g-C_3N_4 and improved the photocatalytic activity. It has good stability and can be reused many times	The photocatalytic efficiency under visible light still needs to be improved. The degradation selectivity for some contaminants is not high enough	54
ZnO: Sr/g-C_3N_4	The band gap was reduced from 3.5 eV to 1.9 eV, and the efficiency of photocatalytic degradation of cationic dye MB (99%) and anionic dye MO (95%) was significantly improved	Green synthesis (using plant extracts) with both antioxidant and anti-diabetic biomedical potential	Toxicity assessment for biomedical applications is inadequate, and further validation of safety is needed	55
Ce/P functionalized g-C_3N_4/ABS nanocomplexes	Significantly improved flame retardancy, thermal stability and mechanical properties for use in engineering plastics	Multi-functional composite materials, breaking through the performance limitations of traditional flame retardants	The effects of environmental ageing in long-term use can be costly for industrial applications	56
Precursor modulation of g-C_3N_4 (U550)	The urea precursor prepared g-C_3N_4 (U550) with the highest N/C ratio (1.22) and RhB degradation efficiency of 80.27% (100 min)	The performance was optimised by precursor selection and the photocatalytic mechanism was well defined (·OH and h^+ dominated)	Strong dependence on precursor purity and possible feedstock consistency challenges in industrial production	57
Ag-0.8/LaCN-1	The adsorption capacity for methyl orange (MO) was 49.6 times higher than that of bulk g-C_3N_4 (BCN), and the photocatalytic degradation rate was 13.1 times higher than that of BCN.The synergistic effect of La doping and Ag NPs significantly enhanced the adsorption and photocatalytic performance	High specific surface area (48.1 m^2 g^{-1}) and mesoporous structure providing more active sites. Visible light absorption range extended beyond 550 nm (band gap 2.50 eV). Good cycling stability (only 3% decrease in total removal after 5 cycles)	The preparation process involves multiple steps (pyrolysis + wet impregnation) and is more complex. The leaching of trace amounts of Ag (0.25%) and La (0.01%) may pose an environmental risk	58
g-C_3N_4/FTO glass composite film and g-C_3N_4/Si composite film	Powdered g-C_3N_4 degraded 96.3% of rhodamine B (Rh B) in 8 h, while LB film degraded 73% in the same time. The LB film after repeated use (after 24 h) maintained 73% degradation efficiency	Remarkable photocatalytic performance, material stability Lianghao FTO glass on the LB film coverage uniform, after repeated use still maintains stable activity. LB technology can be accurately regulate the film thickness and structure, suitable for photoelectric devices and chemical conversion system integration, synthesis of raw materials is cheap and easy to obtain, suitable for large-scale applications	Incomplete coverage (presence of voids) on a silicon substrate limits its application on that substrate. The degradation efficiency of the LB film was reduced compared to the powder (73% *vs.* 96.3%), probably due to the reduction of active sites as a result of unilateral contact of the film with the substrate	59
Co_2SiO_4/g-C_3N_4	The highest degradation rate of EB under UV light (90%, within 120 min) was significantly better than that of single components (57.7% for pure g-C_3N_4 and 63.6% for pure Co_2SiO_4). The catalytic efficiency only decreased by 11.1% after 5 cycles of use	Simple preparation process, low cost, suitable for large-scale production. The performance remains stable after many cycles, suitable for long-term application. It can effectively remove organic dye pollutants in water and is suitable for sewage treatment	Low utilisation of visible light, limiting practical application scenarios. Degradation of anionic dyes is significantly better than that of cationic dyes, limiting the scope of application. The optimal degradation requires 70 mg of catalyst (0.7 g L^{-1}), which may increase the cost, and	60

Table 1 (*Contd.*)

Materials	Findings	Advantage	Disadvantage	Ref.
			the long-term use of cobalt in Co_2SiO_4 may pose a risk of metal leaching	
Pt/CuPc/g-C_3N_4 Z-type heterojunction	Under visible light, the Pt/CuPc/g-C_3N_4 catalysts selectively reduced CO_2 to CH_4 in yields of 39.8 μmol g^{-1} h^{-1}, with selectivities of up to 90%, which were significantly better than those of the single components (pure g-C_3N_4 and CuPc yields of 15.9 μmol g^{-1} h^{-1} and 12.8 μmol g^{-1} h^{-1}, respectively). After 12 h of continuous reaction and 5 cycles, the catalytic activity only decreased by 11.1% without significant structural degradation	The introduction of CuPc extends the light absorption range to the near-infrared region (800 nm) and enhances the solar energy utilisation, while the Z-type heterojunction structure significantly reduces the charge complexation rate and enhances the photocurrent intensity	The high cost of precious metal Pt as a co-catalyst limits the economics of large-scale applications. Involving multiple steps (ultrasonic dispersion, photodeposition of Pt, *etc.*), the process conditions need to be precisely controlled, which may increase production costs. The optimal CuPc loading is 5 wt%, and excessive amounts (*e.g.*, 10 wt%) can lead to active site blockage and performance degradation. Long-term use of Pt and Cu may lead to metal leaching, and the environmental safety needs to be further evaluated	61
MoS_2@g-C_3N_4	MoS_2@g-C_3N_4 adsorption efficiency: RhB (pH 4.0): 96%, SLD (pH 8.0): 96%, FLX (pH 9.0): 85%, with good photocatalytic degradation ability, and the photocatalytic efficiency remained 99–100% after 5 cycles. The BET surface area amounted to 69.53 m^2 g^{-1}, with a significant increase in pore volume	Combined adsorption and photocatalytic degradation capabilities, enhanced adsorption capacity and reactive sites. The performance does not decay after many cycles and is suitable for long-term application. g-C_3N_4 is a metal free material with high chemical stability. Adsorption efficiency for different pollutants can be optimised by adjusting pH	Excess MoS_2 covers the g-C_3N_4 surface, leading to loss of photocatalytic activity. The adsorption efficiency (85%) for FLX is lower than that of RhB and SLD. the degradation time is longer and the synthesis is complicated, which requires precise control of the ratio of MoS_2 to g-C_3N_4 and the synthesis conditions	62
Pd SAs/g-C_3N_4	The photocatalytic hydrogen production efficiency reached 0.24 mmol h^{-1} mg^{-1} Pd at a Pd loading of only 0.05 wt%, which is 55 times higher than that of conventional Pd nanoparticles (1.5 wt%). After five cycle tests, the catalytic activity remained stable (99–100%) without Pd atom agglomeration or deactivation	Only 0.05 wt% Pd loading is required for significant cost reduction. The single-atom active site maximises atom utilisation and avoids agglomeration of nanoparticles. The Pd–N coordination structure significantly reduces R_{ct} and reduces photogenerated carrier complexation. The Pd loading is adjusted by precursor concentration, and the process is simple and reproducible. Efficient hydrogen production under visible light (365 nm) for practical photocatalytic systems	Only $Pd(NH_3)_4Cl_2$ achieves efficient monoatomic dispersion, and other precursors (*e.g.* $PdCl_2$) are prone to nanoparticle formation or incomplete reaction. Pd loading above 0.26 wt% decreases the activity due to atomic agglomeration. Excellent performance under laboratory conditions, but the problems of homogeneous dispersion and cost control need to be solved in large-scale production	63
CuO/Fe_3O_4@ g-C_3N_4 double-Z ternary composites	The use of Aloe vera extract as a reducing and stabilising agent resulted in the formation of a double Z-type heterojunction, which significantly reduced the	Using an environmentally friendly process, the quantum dot sizes of CuO and Fe_3O_4 (~3.34 nm) enhance light absorption and surface reactivity. The	The synthesis conditions are harsh and the composites are stuck in the laboratory stage. Data on photocatalytic efficiency or material structural stability after	64

Table 1 (*Contd.*)

Materials	Findings	Advantage	Disadvantage	Ref.
	band gap energy (from 2.66 eV to 1.67 eV for g-C_3N_4) and broadened the visible light absorption range. The photogenerated electron–hole pair complexation rate of the composites was significantly reduced, the charge transfer resistance (R_{ct}) decreased, and the specific surface area was 74.5 m^2 g^{-1} with a pore size distribution of 12.1 nm, providing abundant active sites	charge separation is facilitated by a double Z-type heterojunction mechanism to enhance the photocatalytic redox capability. Absorption in the UV to visible light range, suitable for practical environmental applications	multiple cycles of use are not available, and performance comparisons with traditional non-biobased materials (*e.g.*, Pt/g-C_3N_4) are lacking, making it difficult to comprehensively assess competitiveness	
Ternary CuO/ZrO_2@S-doped g-C_3N_4 hybrid nanocomposites	The introduction of S doping and CuO/ZrO_2 significantly optimised the grain size of g-C_3N_4 and enhanced the crystallinity, with a significant reduction in the photogenerated electron–hole pair complexation rate, excellent electrocatalytic performance, and a low limit of detection (LOD) as low as 1.7 μM and a limit of quantification (LOQ) as high as 2.1 μM when used for bisphenol A (BPA) detection	High electrocatalytic activity and selectivity, inexpensive raw materials, simple synthesis method and high yield, both photocatalytic and electrochemical sensing potential, suitable for environmental remediation and pollutant detection, improved thermal stability	The proportion of sulphur doping and metal oxide loading needs to be precisely controlled, and the metal oxides may agglomerate in long-term use, affecting the performance	65
Heterojunction of S-type $NiMn_2O_4$/g-C_3N_4 nanocomposites	Under visible light, 1% $NiMn_2O_4$/g-C_3N_4 degraded EB at 10 ppm by 96.41% (120 min) with a rate constant k = 0.0241 min^{-1}. The degradation efficiency decreased by only 10.17% after 5 cycles, showing good stability	The degradation rate of EB under acidic condition (pH = 4) was up to 96.41%, and showed degradation potential for many organic dyes (*e.g.* rhodamine B, methyl violet, *etc.*), with inexpensive raw materials (*e.g.* nickel nitrate, manganese nitrate, melamine) and simple process	Elevated pollutant concentration (*e.g.*, 30 ppm EB) led to a significant decrease in degradation (from 96.41% to 47.46%), a substantial decrease in degradation efficiency (63.09%) under alkaline conditions (pH = 10), and a decrease in the photocatalytic performance after $NiMn_2O_4$ loading of more than 1%	66
SiO_2@g-C_3N_4/Au NPs	Au NP broadens the visible light absorption range and promotes photogenerated electron–hole pair separation through the formation of Schottky barriers. Silicon dioxide nanotubes provide high specific surface area (BET surface) and mesoporous structure to enhance contaminant adsorption. The band gap decreased from 2.71 eV in pure g-C_3N_4 to 2.63–2.69 eV (after modification by Au NPs), but was still higher than the ideal semiconductor band gap (2.0 eV)	The degradation kinetic constant of SiO_2@g-C_3N_4/Au 0.5% (0.0068 min^{-1}) was significantly higher than that of pure g-C_3N_4 (0.0019 min^{-1}), and silica nanotubes were derived from the natural eolianite clay, the synthesis process is green and less costly, and the LSPR effect of Au NPs enhances visible light absorption and reduces the dependence on UV light	The use of gold nanoparticles increases the material cost and the loading needs to be strictly optimised. The band gap is still high (2.63–2.71 eV) and the efficiency of utilising the solar spectrum is limited. Multi-step synthesis is involved and the process is difficult. Both SiO_2 and g-C_3N_4 are negatively charged at near-neutral pH, inhibiting the adsorption of negatively charged pollutants	67

assisted by microwave,[40] and solvent thermal method.[39] In recent years, photocatalytic technology has emerged in the field of purifying mycotoxins in food and the environment.[41,42] g-C_3N_4, as an innovative nonmetal semiconductor material, is capable of stimulating the production of photogenerated electrons and holes when exposed to visible light and then trigger a redox reaction. This property has garnered considerable interest in the field of photocatalytic studies. Through its ability to combine with other functional materials, g-C_3N_4 can form nanogel composites with strong synergistic effects, which perform excellently in improving the adsorption and photocatalytic degradation capabilities of PAT.

Additionally, particle size significantly influences the photocatalytic performance of g-C_3N_4. Smaller particle sizes enhance the dispersibility of g-C_3N_4, exposing a higher density of active sites and facilitating the separation/migration of photogenerated charge carriers. This synergistic effect substantially boosts its capacity for photocatalytic hydrogen peroxide (H_2O_2) generation and organic pollutant degradation. As demonstrated by Zhang *et al.*, g-C_3N_4-KCl synthesized *via* a salt-templating approach exhibits the smallest particle size and superior dispersibility compared to its non-templated counterpart. Notably, its H_2O_2 production rate reaches 6.32 mmol g^{-1} h^{-1}, 32-fold higher than that of non-salt-templated g-C_3N_4.[43] Moreover, g-C_3N_4-KCl achieves a degradation rate constant (k) of 0.1707 min^{-1} for rhodamine B (RhB) under visible light irradiation, doubling the performance of non-templated g-C_3N_4 and demonstrating exceptional photocatalytic degradation efficiency.

There have been reports of methods for degrading mycotoxins in food *via* photocatalytic techniques, with PAT being mentioned as one of the target toxins.[44,45] For example: under ultraviolet irradiation, N-TiO_2 nanoparticles (Nps) exhibit excellent photocatalytic activity, which can completely remove PAT in simulated juice and natural juice within 1 hour. Ultraviolet irradiation promotes the generation of degradation active sites in N-TiO_2Nps, and the properties of these active sites are heterogeneous.[45] A La-$ZnFe_2O_4$@Fe_3O_4@carbon magnetic hybrid material was successfully prepared through a straightforward absorption–pyrolysis method, utilizing a MOF (Zn, Fe) as the starting material. Under ultraviolet light, the composite material possesses the advantage of a large surface area per unit mass and superior photocatalytic capabilities and has a particularly significant degradation effect on aflatoxin B_1, PAT and zearalenone, with degradation efficiencies as high as 98.37%, 97.35% and 98.52%, respectively.[46]

Compared with other treatment methods, photocatalytic technology has shown unparalleled advantages in removing mycotoxins, including the use of clean and pollution-free solar energy, efficient degradation of pollutants under mild conditions, and complete harmlessness of pollutants. Treatment, as well as the high efficiency, stability and recycling of photocatalysts. Therefore, photocatalytic technology provides a completely novel approach for the purification of mycotoxins in food and the environment.[47] Nevertheless, one major drawback of photocatalytic reactions lies in their lack of selectivity. This implies that should photocatalytic technology be directly utilized in the food industry, it will likely lead to the destruction of food nutrients unavoidably. Photocatalysts, as core elements in the photocatalytic process, have a decisive influence on the reaction performance. The early research regarding the photocatalytic regeneration of adsorbents in the environmental domain has offered fresh concepts and inspiration for the transformation of photocatalysts.[48,49]

However, because g-C_3N_4 is hydrophobic, agglomeration is very likely to occur in practical applications. This agglomeration not only exerts an adverse effect on the photocatalytic properties of the material but also exacerbates the recombination of electrons and holes.[50] To solve this problem, we can learn from the modification ideas of graphene oxide, and through a series of

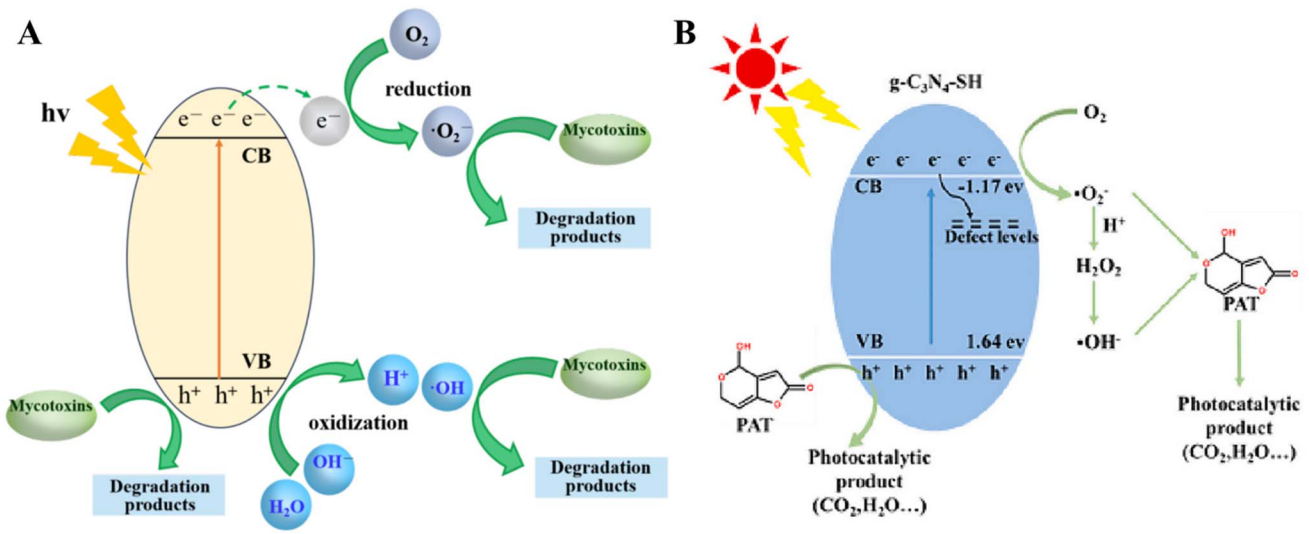

Fig. 4 Schematic of a typical photocatalytic mechanism. (A) Schematic representation of a typical photocatalytic mechanism;[68] (B) schematic representation of the photocatalytic mechanism of KG-5 photocatalyst.

modification methods, hydroxyl and carboxyl groups are introduced at the exterior of g-C_3N_4 to increase its hydrophilicity and effectively reduce agglomeration in water, further improving its photocatalytic performance.[51–53]

Although g-C_3N_4 has certain advantages in the field of photocatalysis, it inevitably has some inherent defects. For example, its electron–hole recombination rate is high, its absorption capacity is insufficient for observing light, its surface reaction kinetics are slow, and the surface area in contact with the catalyst and the reactants is limited, resulting in incomplete adsorption of pollutants and a relatively large number of active sites wait less.[22] To overcome the above shortcomings, it is particularly important to explore appropriate strategies to improve the photocatalytic performance of g-C_3N_4.

Mycotoxins, as a class of highly toxic secondary metabolites, pose significant risks to food safety, ecological safety and public health. Nano semiconductor photocatalytic technology is regarded as a highly promising degradation strategy, and its application in g-C_3N_4-based composites is particularly noteworthy (Table 1). Due to the high performance, cost-effectiveness, and environmental friendliness of g-C_3N_4-based composites, they exhibit unique advantages in the field of mycotoxin abatement. In order to enhance the practical application of the adsorption and degradation system, it is necessary to systematically analyse the key influencing factors, such as the energy band structure of the photocatalysts, the molecular characteristics of the pollutants and the reaction conditions, so as to optimize the degradation pathway and reaction kinetics.

Adsorption enriches the target molecules on the catalyst surface, shortening the mass transfer distance between the photogenerated carriers and the contaminants and improving the reaction kinetics. Adsorbed contaminants can act as electron acceptors (or donors) to facilitate photogenerated carrier separation. For example, adsorbed O_2 molecules trap electrons to generate $\cdot O_2^-$, while organic pollutants act as hole traps to reduce e^-–h^+ complexation. High surface concentration of pollutants can accelerate the chain reaction process of photocatalytic reaction, which is especially effective for difficult-to-degrade pollutants (*e.g.*, antibiotics, perfluorinated compounds).

Photocatalysis enhances the adsorption capacity, under light, photogenerated holes (h^+) positively charge the surface of the material and enhance the adsorption of anionic pollutants, while photogenerated electrons (e^-) reduce the adsorption sites and promote the adsorption of cations. The photocatalytic reaction may change the molecular structure of pollutants to generate intermediates that are easier to adsorb, or change the valence state of pollutants through redox to enhance the subsequent adsorption efficiency. After photocatalytic degradation of adsorbed pollutants, the adsorption sites are released to achieve *in situ* regeneration of the material, avoiding the saturation problem of traditional adsorbents. For example, phenol adsorption was photocatalytically mineralised to CO_2 and H_2O, and the surface active sites were restored.

Fig. 4A illustrates a typical photocatalytic process. Following the efficient transfer of photogenerated charge carriers to the semiconductor surface, electrons (e^-) interact with oxygen (O_2) to produce superoxide radical anions ($\cdot O_2^-$). These radicals can undergo protonation leading to the formation of superoxide hydroxyl radicals (–HOO) and the subsequent production of hydrogen peroxide (H_2O_2). Superoxide and hydroxyl radicals contribute significantly to the degradation of mycotoxins. Meanwhile, holes (h_{VB}^+) can directly oxidise mycotoxins to form degradation products or react with water (H_2O) to produce hydroxyl radicals ($\cdot OH$). g-C_3N_4-SH@KG achieves efficient removal of PAT and regeneration of the material through the synergistic effect of efficient adsorption of thiol groups and photocatalytic regeneration by the mechanism shown in Fig. 4B. The thiol functionalisation not only the thiol functionalization not only enhances the adsorption selectivity, but also optimizes the photocatalytic activity, and the "dark adsorption–photoregeneration" strategy takes into account the food safety and sustainability of the material, which provides a new idea for the control of food contaminants.[68]

Synergistic structural modulation strategies to construct meso/macroporous structures by templating or thermal stripping to enhance mass transfer efficiency and adsorption

Table 2 Performance data of modified g-C_3N_4

Modification method	Performance parameter	Performance data	Ref.
Nitrogen doping	Band gap (eV)	2.7	78
Nitrogen doping	Specific surface area ($m^2\ g^{-1}$)	1500	79
Nitrogen doping	Photocatalytic H_2 evolution rate ($\mu mol\ g^{-1}\ h^{-1}$)	100	79
Nitrogen doping + metal doping	Photocatalytic H_2 evolution rate ($\mu mol\ g^{-1}\ h^{-1}$)	220	78
Carbon doping	Band gap (eV)	2.2	78
Carbon doping	Photocatalytic H_2 evolution rate ($\mu mol\ g^{-1}\ h^{-1}$)	180	78
Co, Ni doping	Electrocatalytic HER activity (mV)	150	79
Co, Ni doping	Electrocatalytic HER activity (current density, $mA\ cm^{-2}$)	10	79
Molybdenum doping (Mo)	Photocatalytic H_2 evolution rate ($\mu mol\ g^{-1}\ h^{-1}$)	300	79
Molybdenum doping (Mo)	Photocatalytic CO_2 reduction rate ($\mu mol\ g^{-1}\ h^{-1}$)	70	78
Surface modification (polymer)	Specific surface area ($m^2\ g^{-1}$)	1700	79
Surface modification (oxidation)	Photocatalytic H_2 evolution rate ($\mu mol\ g^{-1}\ h^{-1}$)	150	78
Nanostructuring	Photocatalytic H_2 evolution rate ($\mu mol\ g^{-1}\ h^{-1}$)	500	78
Nanostructuring	Photocatalytic CO_2 reduction rate ($\mu mol\ g^{-1}\ h^{-1}$)	90	78

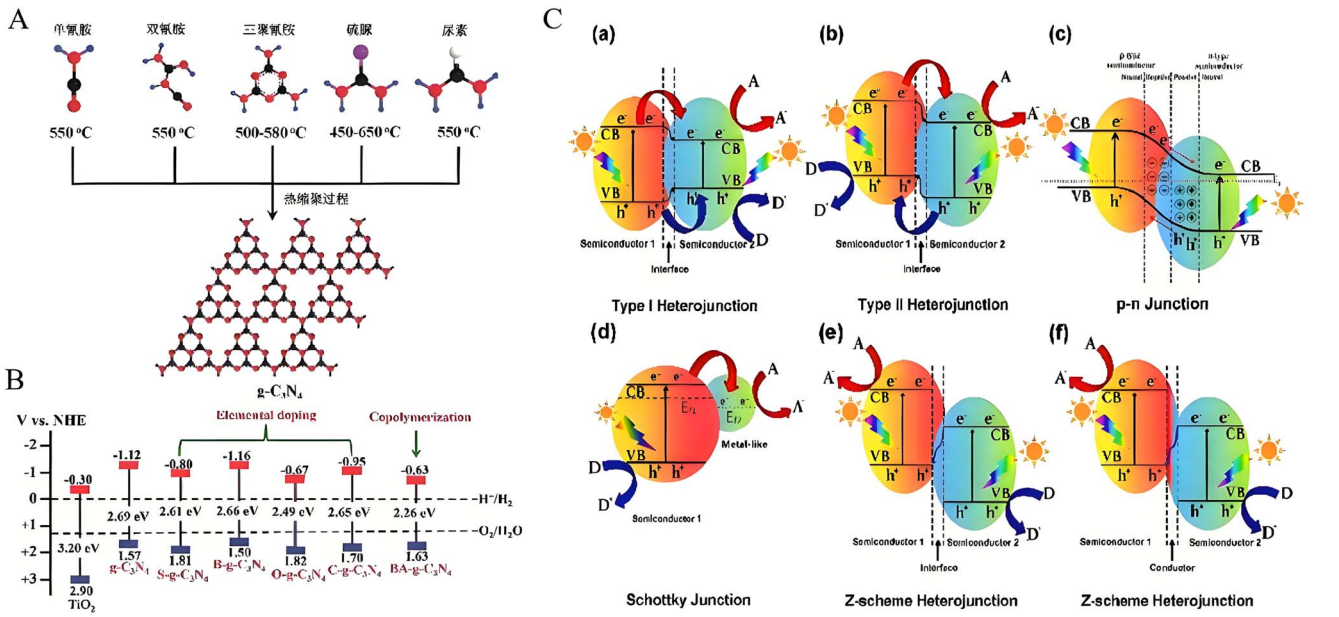

Fig. 5 Energy band structure of doped g-C_3N_4 synthesized by thermal polycondensation. (A) g-C_3N_4 was synthesized from several precursors by thermal polycondensations.[80] (B) Energy band diagrams of TiO_2 and g-C_3N_4, along with their commonly used dopant species.[80] (C) Illustrative representation of the energy band configure uration of various types of heterojunctions.[81]

capacity (three-dimensional porous g-C_3N_4). Introducing electron-rich groups to enhance the selective adsorption of specific pollutants. Load co-catalysts to facilitate photo-generated carrier separation while providing additional adsorption sites. Formation of heterojunctions with semi-conductors (TiO_2, BiOBr) or conductive materials (graphene) to optimise the light absorption range and enhance interfacial adsorption-catalysis synergies.

Porous materials (*e.g.*, graphene hydrogel, g-C_3N_4-HEC hydrogel, TiO_2/g-C_3N_4) enrich pollutants (*e.g.*, BPA, PAT) through physical and chemical adsorption, and shorten the mass-transfer distance between the photogenerated carriers and the pollutants; heterojunction structures (*e.g.*, BiOI/porous g-C_3N_4, TiO_2/g-C_3N_4) promote the charge separation through energy band matching, the photogenerated electrons are transferred to the conducting substrate (graphene) or another semiconductor conduction band, and holes are retained in the valence band, inhibiting compounding and enhancing photo-catalytic activity; adsorbed pollutants act as electron acceptors (O_2 to generate $\cdot O_2^-$) or hole trappers (direct oxidation), and efficient degradation is achieved by ROS; pollutants are mineralised into harmless products after photocatalytic reaction (CO_2, H_2O) after the photocatalytic reaction, releasing the adsorption sites to achieve *in situ* regeneration of the material, while the dynamic flow system (continuous photoreactor) maintains long-term stability through adsorption–degradation rate matching. The synergistic effect is essentially a coupled process of "adsorption enrichment – *in situ* transformation – dynamic recycling", and the efficient removal of pollutants is achieved through the design of multi-stage structure of the material and interface regulation.[69–71]

The synergistic effect of carbon nitride adsorption and photocatalysis is essentially a dynamic coupling process of "enrichment–reaction–regeneration", the core of which lies in the efficient capture and rapid transformation of pollutants on the surface through the design of materials and interface regulation. In the future, we need to further combine *in situ* characterisation to reveal the synergistic mechanism at the molecular level and to promote the precise design for practical applications.

2.2.3 Modification of graphite phase carbon nitride. When designing efficient g-C_3N_4-based photocatalysts, researchers have proposed the following modification strategies (Table 2): constructing heterojunctions. After different semiconductor materials form heterojunctions, they are energy-saving. The difference in band structure enables the promotion of the directional transfer of photogenerated carriers at the interface. This effectively suppresses charge recombination, brings about a significant improvement in the effectiveness of charge transfer migration and separation and hence, improves the photo-catalytic performance.[72] Dimension adjustment, such as the conversion of bulk phase materials into 2D nanosheets or one-dimensional nanostructures, can significantly increase the surface area per unit mass, shorten the pathway for carrier transport path, accelerate charge movement and division, and enhance the efficiency of photo-catalytic processes;[73] loading of suitable cocatalysts into g-C_3N_4. Precious metals like Au and Pt are utilized as cocatalysts by depositing them onto the surface. These precious metals have high electron mobility and can quickly capture photogenerated electrons, act as electron absorbers, minimize the reconnection of electrons and holes, and concurrently, serve as reduction-promoting cocatalyst, reduce the reaction activation energy, accelerate the process of

reduction reactions, serve as photosensitizers, expand the absorption range of visible light, enhance the response ability of g-C_3N_4 to visible light;[74,75] surface defect control introduces appropriate amounts of defects, such as nitrogen vacancies, on the exterior of g-C_3N_4 through physical or chemical methods. These defects can become additional active sites, accelerating surface reaction kinetics and increasing the likelihood that photogenerated carriers will participate in surface reactions, thereby improving charge utilization and improving photocatalytic activity,[76] morphology adjustment, surface sensitization and energy band regulation, *via* morphological adjustment, such as the preparation of porous structures or nanoflower-like g-C_3N_4, increase light scattering, extend the optical path, and improve the light absorption efficiency. In addition, g-C_3N_4 was synthesized using the thermal polycondensation method (Fig. 5A). Surface sensitization involves modifying a sensitizer with a suitable energy level on the outer layer of g-C_3N_4 so that the sensitizer absorbs light and transfers excited electrons to the conduction band of g-C_3N_4, thereby widening the spectrum of light absorption. Energy band regulation modifies the energy band configure uration of g-C_3N_4 through element doping and other means so that the light that absorbs edges redshifts, absorbs more long wavelength light, and improves photocatalytic activity in all aspects.[77]

(1) Energy band regulation

The most prevalent modification approach for enhancing the capability of g-C_3N_4 to absorb visible light is to carry out energy-band engineering. By adjusting the components or morphology, the position of the semiconductor catalyst bottom or apex of the valence energy band is capable of being adjusted so that the visible light absorption band edge of the catalyst redshifts, thereby expanding its visible light response wavelength range. Furthermore, energy band engineering has the capacity to enhance the oxidation–reduction capabilities of the catalyst. By doing so, it offers a more potent driving force for the target oxidation–reduction reaction, thereby augmenting the catalytic activity of the catalyst.[82]

In the current energy band regulation research on g-C_3N_4, element doping is one of the most in-depth and widely used methods, covering two directions: metal element doping and nonmetal element doping. At this stage, in terms of bandgap regulation, the incorporation of metal elements is the most effective method and is widely used to regulate the arrangement of electrons and optical attributes of g-C_3N_4. The catalytic ability of g-C_3N_4 can be significantly improved by incorporating different transition metal ions into its structure. These ions of transition metals encompass Zn^{2+}, Mn^{3+},Fe^{3+}, Ni^{3+}, Co^{3+}, as well as Cu^{2+}.[83–86]

As depicted in Fig. 5B, apart from the doping of metal elements, the doping of non-metallic elements like S, B, O, and C can also decrease the energy gap of g-C_3N_4. This reduction in the band gap leads to an improvement in its light absorption performance and an enhancement in the degree of delocalization of conjugated electrons.[87–90] Through a blend of experimental and theoretical approaches, Liu and colleagues verified that the incorporation of P can substitute for C_1 or N_2 positions, effectively narrowing the forbidden bandwidth of g-C_3N_4 to 2.20 eV. Moreover, the doping of P is highly important for the movement and partitioning of light-induced electrons.

(2) Porous structure design

Creating a porous structure for g-C_3N_4 provides numerous advantages. For one thing, it can increase the catalyst's specific surface area directly and enhance its pore volume. Consequently, its adsorption performance is notably enhanced; on the other hand, it also has the ability to elevate the count of reactive sites. This effectively propels the progression of surface reactions, speeds up the electron migration and separation process, and at the same time, elevates the light collection efficiency.[91] When preparing porous g-C_3N_4 nanophotocatalysts, a variety of soft template methods have been used, such as ionic liquids,[92] bubble templates,[93] *etc.* However, ionic liquids have obvious disadvantages, their cost is high, their carbon residue is high, and they are insoluble in water. These disadvantages seriously restrict their promotion in large-scale practical applications.

To overcome these shortcomings of the soft template method, researchers have conducted many in-depth studies on the hard template method.[94] Theoretically, from the perspective of principles, any material featuring an ultra-high specific surface area can be utilized as a hard template for the preparation of g-C_3N_4. At present, many related studies have reported successful preparation methods, such as the use of porous alumina,[95] SiO_2,[96] SBA15,[97] *etc.* as hard templates. Among these materials, the mesoporous SiO_2 is the most commonly used hard template. Due to its distinctive structure and characteristics, it serves as an outstanding template to facilitate the formation of porous structures in g-C_3N_4.

(3) Shape adjustment

Nanosized g-C_3N_4 exhibits more prominent advantages in photocatalysis compared to bulk g-C_3N_4. Due to its larger specific surface area, it can offer a greater number of reaction sites; shorter charge migration distances, allowing photogenerated carriers to reach the reaction site faster; and higher solubility, which helps in the reaction system. Evenly dispersed and has an adjustable energy band structure.[98] In particular, the distance that photogenerated carriers need to travel in g-C_3N_4 is significantly shorter compared to bulk material, allowing them to readily reach the catalyst surface for reaction, thus enabling efficient separation of photogenerated electron–hole pairs. This resulted in a substantial enhancement in photocatalytic efficiency.

To date, in the domain of photocatalysis, a wide variety of g-C_3N_4 nanostructures with diverse morphologies have undergone extensive development and utilization. These encompass 0D quantum dots or nanoparticles, 1D nanowires, nanorods, or nanotubes, 2D nanosheets or nanothin films, as well as 3D hierarchical architectures.[99–103] Owing to their unique surface properties, 2D ultrathin g-C_3N_4 nanosheets and 0D nanoparticles provide many adsorption and reaction sites for reactant molecules. 0D and 2D materials, due to the influence of dimensional effects, not only have an increased specific surface area, enabling them to offer more adsorption and reactive centers, but also lead to a reduction in the interface energy barrier. This reduction improves the carrier transmission

efficiency and significantly shortens the transmission path; thus, the overall photocatalytic activity has been comprehensively improved, making broader application prospects in the field of environmental purification.[104]

(4) Constructing heterojunctions

The construction of heterojunctions with other materials effectively enhances the catalytic performance of g-C_3N_4 semiconductors under light illumination. This happens due to the fact that, upon the recombination of two semiconductors, an electrical field inside arises between them. This internal electrical field aids in the swift dissociation of electrons and holes. Consequently, the rate at which photogenerated charge carriers recombine is reduced, and their lifetime is prolonged. As presented in Fig. 5C, the mechanisms by which charge carriers are separated in heterojunctions can be categorized as follows: type I, type II, p–n junctions, Schottky junctions, and Z-scheme heterojunctions.[105]

In the structure of a type I heterojunction that is established, both electrons and holes accumulate in one of the semiconductors, which decreases the likelihood of electron–hole recombination occurring in the other semiconductor. In the case of a p–n heterojunction, electrons migrate from the conduction band of the p-type semiconductor to that of the n-type semiconductor, while concurrently, holes shift from the valence band of the n-type semiconductor to the valence band of the p-type semiconductor, thereby realizing efficient electron–hole separation. The mechanism for charge transfer involving type II heterojunctions is similar to that of type p–n heterojunctions. Schottky junctions are usually heterogeneous interfaces formed by metals and semiconductors. The Z-type heterojunction not only efficiently achieves charge carrier isolation but also preserves the strong oxidation and reduction potentials of the two semiconductors and has excellent oxidation and reduction powers.

Cai and colleagues managed to synthesize g-C_3N_4/CuS p–n-type heterojunction photocatalysts *via* an *in situ* synthesis method. Experimental results indicated that the degradation rates of RhB and MB for this combination were 8.91 times and 13.54 times higher, respectively, compared to pure g-C_3N_4, and 3.02 times and 6.37 times higher, respectively, compared to pure CuS. The key factor for boosting the efficiency of catalysis of g-C_3N_4 under light exposure the lies in the adaptation of the energy band position of CuS to that of g-C_3N_4. Additionally, it offers more interfaces in order to facilitate the high-efficiency transfer of photo-created electron–hole pairs, thus suppressing recombination.[81]

For all kinds of heterojunctions, tight interface contact is an important guarantee for the effective transmission of electrons.[106] Cao *et al.* used a high-energy ball mill-assisted calcination method to prepare a heterojunction composed of multilayer Ti_3C_2 as a support loaded with g-C_3N_4 and oxidized TiO_2 *in situ*. The degradation rate of methyl orange in the ternary Z-type heterostructure is 3.62 times higher in comparison to g-C_3N_4, it is higher, and it is 6.60 times greater than that of Ti_3C_2. These authors hold the view that the improvement in photocatalytic performance stems from the compact Z-shaped heterointerface established among multilayer Ti_3C_2, the enhancement in photocatalytic performance is attributed to porous g-C_3N_4 sheets possessing substantial specific surface areas, as well as TiO_2. This heterointerface promotes the creation of photogenerated carriers within the composite materials. Furthermore, it enhances the dissociation of carriers generated by light and accelerates the advancement of catalytic reactions.[107]

Overall, building heterojunctions with other materials is still the most effective way to optimize g-C_3N_4 photocatalytic properties. On the one hand, the establishment of heterojunctions helps to improve the stability of the catalyst and reduce photocorrosion and agglomeration; on the other hand, there is a synergistic effect between different semiconductors, thereby expanding the spectrum of light absorption and enhancing the efficiency of sunlight utilization. In addition, semiconductor

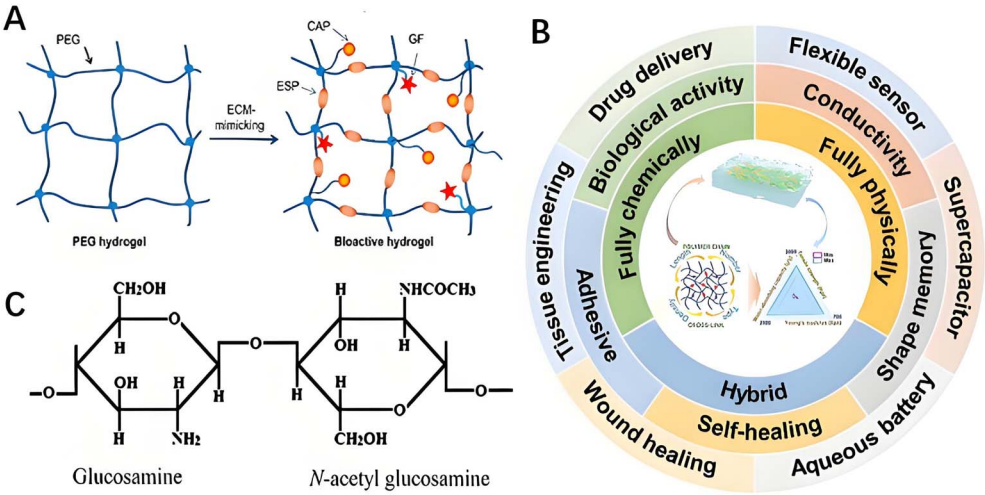

Fig. 6 Structure, modification and application of gels. (A) Chemical structure of chitosan.[130] (B) The structures, characteristics and utilizations of hydrogels. (C) Bioactive modification of PEG hydrogels.[125]

Table 3 Chitosan hydrogels crosslinked with glutaraldehyde can be modified by polymers

Macromolecule	Alteration in properties subsequent to modification	Employment	Ref.
Gelatin	Enhancement of rigidity	Caffeine-specific carriers in the human organism	136
Starch	The flexibility and elasticity of the patch were enhanced, along with the manifestation of favorable bioadhesive properties	The controlled-release delivery of α-hydroxy acid present in the extract of tamarind fruit pulp	137
Hydroxyethyl cellulose	Constructs firm network	Sustained-release delivery of chlorothiazide	138
Polyethylene glycol	Enhances heparin's blood-compatibility and anti-coagulation ability	Research on compatibility for diverse biomedical uses	139
Polyvinyl pyrrolidone	Boosts pH-dependent swelling, creates a firm network	A sustained-release system for delivering amoxicillin	140
Poly(ethylene-*graft*-acrylamide)	Constructs a firm network	Sustained release of capecitabine	141
Poly(acrylic acid-*co*-acrylamide)	Enhances mechanical strength, mucoadhesive ability and solubility	Promising muco-adhesive systems for oral administration of peptide and protein drugs	142
Pluronic F127	Network structure turns more inflexible, leading to enhanced drug retention	Regulated delivery of 5-fluorouracil	143
Alginate and N, O carboxymethy chitosan	Electrostatic repulsion among ionized acidic groups enhances swelling characteristic	Targeted protein delivery in the intestinal tract	144
Carboxymethyl hexanoyl chitosan	Level of hexanoyl replacement alters the swelling capacity and solubility	Entrapment of slightly water – soluble drug	145
Carboxymethyl cellulose and chitosan	Generation of polyion complex offers high strength and steadiness	As a drug delivery vehicle	146
Chitosan and poly(vinyl alcohol)	Alteration of chitosan amount in the grafted polymer enhances cell survival probability	Prospective application in diverse biomedical fields	147
Chitosan and gelatin	Stiffness of the matrix went up	Biomedical utilization	148
Chitosan and polyethylene amide	Reduction in drug release speed as cross-linking density rises	Drug delivery utilization	149
Chitin and chitosan	Offers a beneficial environment for the growth of cartilage cells	Culture of bovine knee chondrocytes	150
Chitosan and gelatin	Rise in the pore-size ratio of the scaffolds	Articular cartilage tissue construction	151

crystal structures used to prepare heterojunctions are crucial to the high quantum efficiency of photocatalysts. The difference in the lattice spacing between the two semiconductors may lead to a lattice mismatch at the interface, thereby inhibiting the recombination of carriers.[108]

In promoting the splitting of light-induced charge carriers, photogenerated electrons can be provided by regulating the dielectric properties of the semiconductor catalyst or by constructing an interface electric field or local electric field or perturbing the local space charge distribution. To enhance the separation efficiency of light-excited electron–hole pairs, the driving force for holes to migrate in opposite directions is increased.[109,110] By adjusting the micromorphology of the catalyst, the migration distance for the transfer of light-induced charge carriers can be shortened, or the electrical properties of the catalyst can be optimized to reduce the migration resistance, such as increasing the crystallinity of semiconductor catalysts and forming new common Price bonds or adjusting the electronic structure.[111,112]

The influencing factors of the catalyst surface redox reaction mainly include the quantity of surfactant binding locations on the catalyst, the overpotential of the material, and the adsorption and activation ability of reactant molecules. By loading or doping components with catalytic efficiency, the overpotential of the catalytic agent can be reduced, the surface area can be expanded, and the count of reactive sites can be increased, and the adsorption and activation ability of reactant molecules can be improved, thereby enhancing the surface redox reaction. activity.[113,114]

3 Overview of graphite-phase carbon nitride-based hydrogels

3.1 Overview of hydrogels

Hydrogels are polymeric materials composed of three-dimensional crosslinked networks that can absorb and retain large amounts of water without dissolving, and their properties can be modulated by the preparation process.[115–121] Among them, cellulose-based hydrogels have attracted much attention due to their good hydrophilicity, biocompatibility and degradability.[122,123] By introducing functional molecules such as cell adhesion peptides, enzyme-responsive sequences, or growth factors (Fig. 6A), its cytocompatibility can be further significantly enhanced to achieve specific cell adhesion and controlled degradation, thus overcoming the limitations of traditional PEG hydrogels in cellular microenvironment construction.[124] In addition, cellulose nanocrystals (CNCs) can significantly enhance the comprehensive performance of hydrogels by virtue of their high hydrophilicity, crystallinity, and environmentally friendly properties,[125] as well as two-dimensional materials, such as g-C_3N_4, through hydrogen bonding.[126–129]

Synthetic hydrogels are prepared by physical or chemical cross-linking.[124,131,132] Chemically cross-linked hydrogels form permanent networks due to covalent bonding.[133] The preparation methods include direct crosslinking of water-soluble polymers or hydrophilic modification of hydrophobic polymers followed by crosslinking. In contrast, physical gels usually have inferior mechanical properties to chemical gels due to weaker dynamic cross-linking, but their reversible sol–gel transition properties are more advantageous for specific applications.[134] The crosslinked structure determines the viscoelastic or elastoplastic behavior of hydrogels, while the elasticity of the polymer network directly affects their sol–gel capacity (Fig. 6B).[122,134] The swelling rate, mechanical properties, and degradation behavior of hydrogels can be optimized by adjusting the hydrophilic to hydrophobic ratio, initiator concentration, and reaction conditions (*e.g.*, time, temperature) (Table 3). Semi-synthetic hydrogels combine the bioactivity of natural polymers with the tunability of synthetic materials, which broadens their applications. Among them, smart hydrogels can respond to environmental stimuli such as temperature and pH. Chitosan hydrogels are produced by deacetylation of chitin and their structure contains glucosamine and *N*-acetylglucosamine units (Fig. 6C). Their properties can be optimized by modifications such as ionic cross-linking, graft polymerization, or polyelectrolyte complex (PEC) formation. For example, PMVC/NVP composite hydrogel particles prepared by ionic gelation improved insulin release in acidic environments.[135]

Hydrogels have shown great potential in the fields of agriculture, biomaterials, food industry and regenerative medicine due to their unique properties.[115,134] Among them, polysaccharide-based hydrogels are prominent in wastewater treatment,[123] for example, by embedding functional particles in hydrogel beads for efficient adsorption of heavy metals, dyes or radioactive pollutants.[152,153] In addition, the responsiveness of hydrogels to external stimuli (*e.g.*, temperature, light, pH, enzymes) makes them valuable in environmental sensing, actuation, and self-assembly systems.[134,154] By precisely tuning the mechanical strength, electrical conductivity or self-repairing ability, hydrogel systems based on natural/synthetic polymers can fulfill diverse applications.[115]

3.2 Preparation of graphite phase carbon–nitride based hydrogels

(1) Construction of g-C_3N_4-based hydrogels with a three-dimensional hierarchical framework through nanostructure engineering.[155]

It has rich pore structure with different sizes of voids, which is conducive to the adsorption and transport of substances; it can absorb and retain a large amount of water, and the water content can be as high as 90% or more; it also has good flexibility; using the efficient electron transport ability of g-C_3N_4, and the close contact interface between it and the active substances, it enhances the adsorption, catalytic and photocatalytic activities of g-C_3N_4.[156] The researchers dispersed g-C_3N_4 nanosheets in sodium alginate hydrogels by ionic crosslinking and found that the photodegradation efficiency of the composite hydrogels for organic pollutants was significantly enhanced, indicating that a reasonable embedding method can effectively regulate the dispersibility and interfacial interactions of g-C_3N_4, which can provide a basis for the design of multifunctional hydrogels.[157] For ternary hybrid aerogels containing

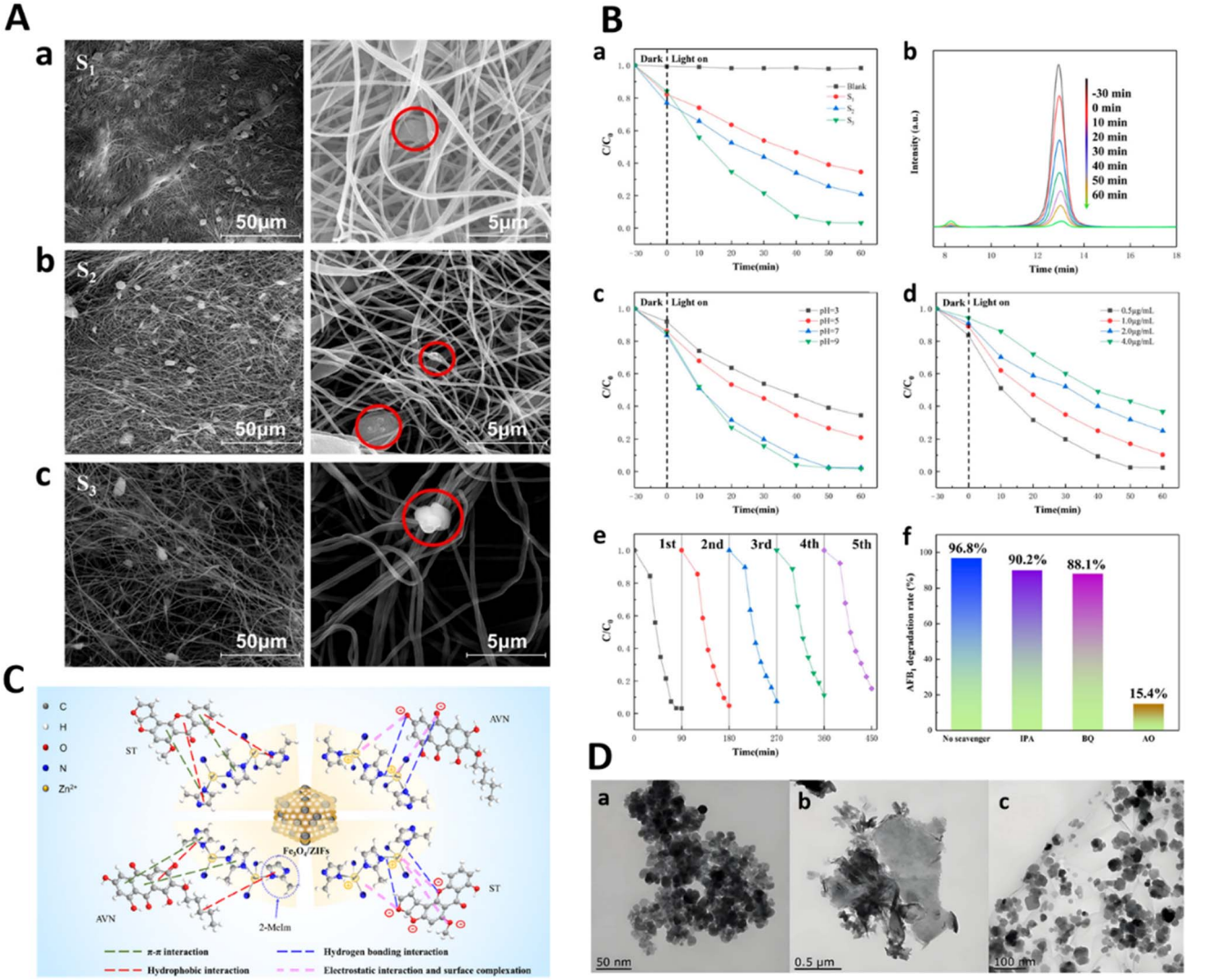

Fig. 7 Characterization, mechanism, catalytic activity diagram of different materials for mycotoxin removal. (A) SEM images of electrospun membranes anchored with g-C_3N_4/MoS_2 prepared by different processes: (a) S_1 ~ mostly wrapped, (b) S_2 ~ partially exposed, and (c) S_3 ~ fully exposed.[158] (B) (a) Photocatalytic degradation efficiencies of AFB_1 with as-prepared S_1, S_2, and S_3 under visible light irradiation. (b) HPLC chromatogram of AFB_1 photocatalytic degradation with S_3 under visible light irradiation at different times. (c) The photocatalytic activity of S_3 for degradation of AFB_1 at different pH values. (d) The photocatalytic activity of S_3 for degradation of AFB_1 with different initial concentrations. (e) The photocatalytic activity of S_3 for degradation of AFB_1 for five cycles. (f) Photocatalytic activities of S_3 for the degradation of AFB_1 in the presence of different scavengers.[158] (C) Extraction mechanism of Fe_3O_4/ZIFs (1 : 8) for AVN and ST.[159] (D) TEM images of Fe_3O_4 (a), g-C_3N_4 (b) and g-C_3N_4/Fe_3O_4 (c) nanocomposites.[160]

g-C_3N_4, GO, metal oxides or layered hydroxides in multicomponent hydrogel composites.[158] DPCN and NiFe-LDH were prepared by calcining urea in argon and hydrogen atmospheres at 550 and 540 °C, respectively, and hydrothermally treating with Ni-based and Fe-based nitrate solutions at 150 °C for 20 h. DPCN/NRGO/NiFe-LDH aerogels were then synthesized by a hydrothermal method in a PTFE-lined autoclave at 180 °C for 6 hours. The hydrogen bonding of amino or hydroxyl functional groups on the surface of g-C_3N_4 with acrylic monomers can be utilized to achieve its homogeneous dispersion and *in situ* polymerization in polyacrylamide hydrogels. In another study, the self-assembly of g-C_3N_4 nanosheets with chitosan was driven by π–π stacking and electrostatic interactions, resulting in the formation of a composite hydrogel with a hierarchical porous structure, which significantly enhances the adsorption capacity for heavy metal ions.

(2) Gelation of g-C_3N_4 derivatives using co-assembly or self-assembly methods.[159,160]

It can be combined with g-C_3N_4 and other materials to form a three-dimensional porous structure while retaining its unique lamellar sp^2 structure. Jiang *et al.* worked on interconnecting GA/GH with g-C_3N_4 using co-assembly or self-assembly methods with the help of internal hydrogen bonding as well as π–π interactions between GA/GH and g-C_3N_4.[148] GA/GH with a three-dimensional porous structure not only provides a large specific surface area, high adsorption capacity, and excellent

mechanical strength, but also forms robust connections and conductive paths during assembly with g-C_3N_4, which in turn enables efficient charge transfer. Qu By calcining hydrothermally treated urea-derived graphene oxide reticulated composites under argon flow at a temperature of 600 °C. A reticulated g-C_3N_4/graphene interconnected mesh network was developed.[144] These samples exhibited mesoporosity with a BET specific surface area as high as 352 m^2 g^{-1} and a pore volume of 1.63 cm^3 g^{-1}, which amply demonstrated that these mesh online structures could significantly facilitate the transfer of water molecules and charges through the porous channels, thus enhancing the activity of hydrogen precipitation reaction. In addition to the hydrothermal assembly of GO with g-C_3N_4, reduced graphene oxide (rGO) also exhibits strong π–π conjugation interactions with g-C_3N_4, which can lead to the formation of g-C_3N_4/rGH hydrogels through the addition of sodium ascorbate as a reducing agent.[150] The BET specific surface area, pore volume, and pore diameter of the 90%-g-C_3N_4/rGH sample were 302.6 m^2 g^{-1}, 1.48 cm^3 g^{-1}, and 3.9 nm, respectively, which suggests that the three-dimensional porous structure facilitates the enhancement of the removal of Cr(VI) by adsorption. Wu *et al.* utilized cetyltrimethylammonium bromide and ethylenediamine with g-C_3N_4 and GO suspension, heated at 95 °C for 7 h, and freeze-dried to obtain functionalized g-C_3N_4/GOA aerogels.[151] This g-C_3N_4/GOA exhibits strong hydrogen bonding interactions, forming a stable structure and abundant three-dimensional connectivity channels for fast charge separation.

(3) The photopolymerisation reaction was used to prepare hydrogels using g-C_3N_4 as an initiator to provide free radicals.

Antonietti *et al.* reported that exfoliated g-C_3N_4 nanosheets can be irradiated with Xenon lamp (lambda >420 nm, 50 mW cm^{-2}) to drive *N*-isopropylacrylamide (NIPAm) cross-linking for free radical polymerization, leading to the construction of PNIPAm/CNNS hydrogels.[139] The concentration of NIPAm and CNNS, radiation duration and energy source (*i.e.*, light or heat) strongly modulated the hydrogelation process. The results showed that the nitrogen atoms of the basic amine used as a co-initiator reacted with the free radicals on the surface of g-C_3N_4, transferring the free radicals directly from the g-C_3N_4 sites to the co-initiator sites, thus initiating the photoinitiated polymerization.

3.3 Application of graphite-phase carbon nitride-based hydrogels

In recent years, several studies have shown that graphite-phase carbon–nitride-based hydrogels combine the advantages of semiconductor photocatalysis and adsorption with porous materials, and exhibit unique potential in the field of adsorption and photocatalytic degradation of PAT.[161–163] Its three-dimensional network structure not only provides abundant active sites, but also significantly improves the photocatalytic performance by enhancing the photogenerated carrier separation efficiency. The swelling property of the hydrogel further enlarges the internal porosity, resulting in a significant increase in the pollutant adsorption capacity compared with that of the conventional powder catalysts.[164] Li *et al.* investigated a novel 3D–2D–3D BiOI/porous g-C_3N_4/graphene hydrogel (BPG) composite photocatalyst synthesized *via* a two-step hydrothermal method, which showed synergistic effects of adsorption and photocatalysis (Fig. 6A).[165] A hydrogel exhibiting selective pollutant adsorption properties was prepared by Sun *et al.* (Fig. 6B).[163,165–167] Fernandes *et al.* proposed the immobilization of g-C_3N_4-T-*N* in sodium alginate hydrogels to significantly improve the efficiency of photocatalytic synthesis of vitamin B3 (VB3). This strategy is promising for the synthesis of VB3, eliminating the need for a photocatalyst separation step, simplifying the reaction flow, efficiently oxidizing the process, targeting the conversion of the intermediate 3PC, and enhancing the pathway controllability. Thurston's group prepared self-supported g-C_3N_4/PVA composite hydrogels by direct casting method. The molecular interactions between the semiconductor particles and PVA chains significantly enhanced the mechanical strength and photophysical properties of the hydrogels when the g-C_3N_4 loading was 0.67% (38% reduction in PL intensity). The dense arrangement of g-C_3N_4 particles at higher loading enlarged the light absorption cross-section by 1.8-fold, and the rate constant of photocatalytic degradation of RhB was increased to 4.3-fold of pure PVA.

4 Application of graphite-phase carbon nitride-based materials

4.1 Application of graphitic carbon nitride-based materials in patulin removal

g-C_3N_4 has become a research hotspot in the field of photocatalysis due to its unique electronic structure and chemical stability, but its specific surface area limitation and charge compounding problems constrain its practical application. g-C_3N_4 is an ideal carrier for modifying g-C_3N_4 by virtue of its high electrical conductivity, large specific surface area, and abundance of functional groups on the surface. Porous g-C_3N_4/GO developed by Sun *et al.* sodium alginate hydrogel microspheres (CN/GO/SA), although focusing on the degradation of aflatoxin B_1 (AFB_1) in peanut oil, the constructed synergistic system of adsorption and photocatalysis provides a universal idea for mycotoxin removal.[157] The g-C_3N_4/MoS_2 composite membrane and magnetic g-C_3N_4/Fe_3O_4 nanomaterials, on the other hand, have been prepared by electrostatic spinning technique to enhance the degradation of AFB_1 in complex food matrices through the enhancement of visible-light responsiveness and the convenient magnetic separation properties, respectively (Fig. 7A and B).[158] Zhang *et al.* studied a controlled magnetic adsorbent Fe_3O_4/ZIFs (Fig. 7C), and found that Fe_3O_4/ZIFs (1 : 8) had the highest adsorption efficiency for two precursors of AFB_1 (AVN, ST) and that the material was also somewhat reusable.[159] On this basis, the TiO_2/g-C_3N_4 composite designed by Yang *et al.* was directly targeted for the efficient removal of PAT, and experiments showed that this heterojunction structure could achieve the complete degradation of 0.5 μg mL^{-1} PAT under 30 °C and 10 mg addition with only 3 min of dark adsorption in conjunction with 5 min of photocatalysis, which is significantly superior to that of the single-component. It was significantly

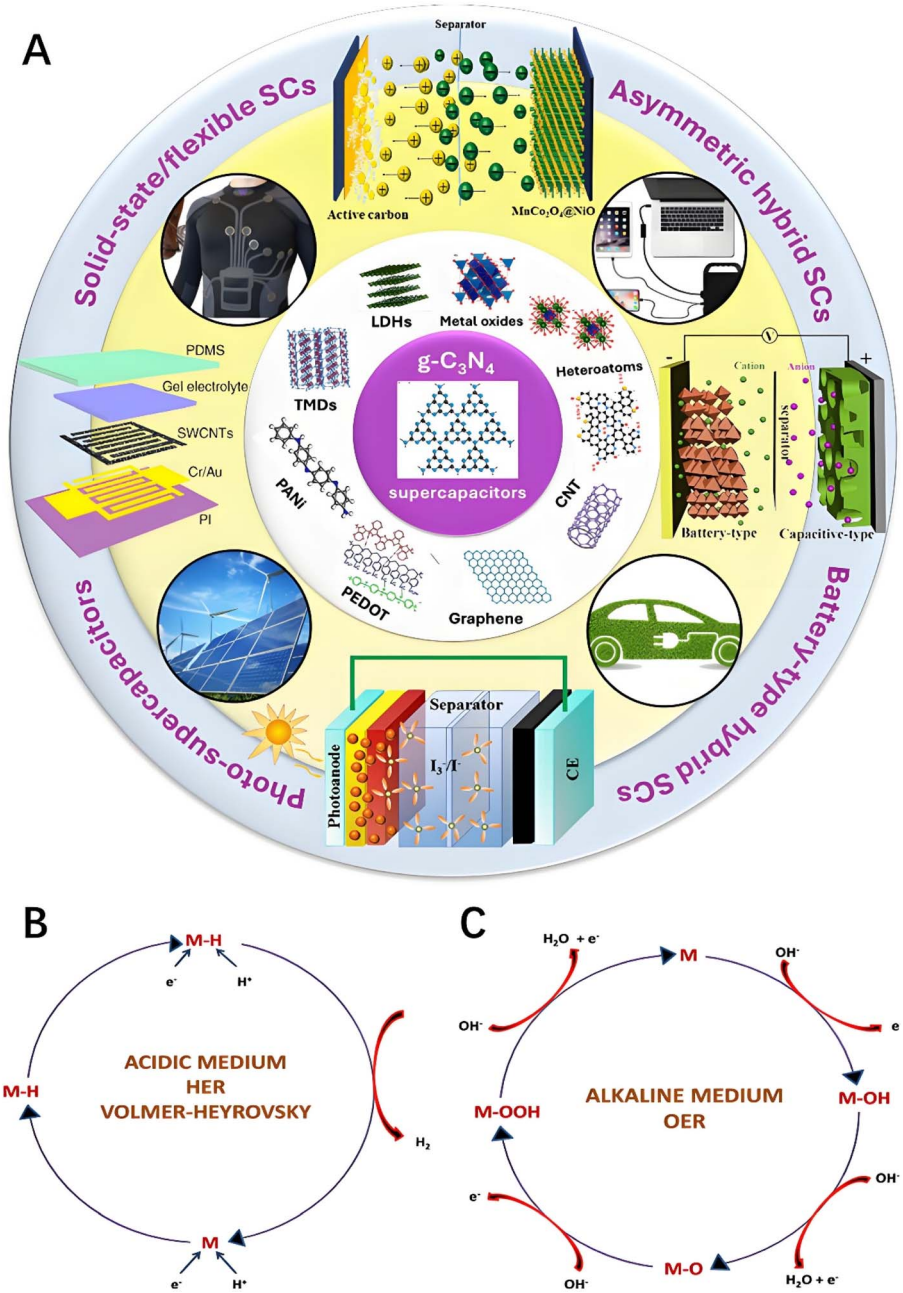

Fig. 8 g-C_3N_4-based materials and electrocatalytic mechanisms for energy conversion applications. (A) Various composites of g-C_3N_4 for supercapacitor applications.[166] (B) Feasible mechanism for the HER. (C) Feasible mechanism for the OER.[165]

better than the adsorption or catalytic performance of single component, revealing the synergistic mechanism of adsorption enrichment and photogenerated carrier separation.[168]

To address the complex contamination scenario of PAT in food matrices such as fruit juices, the nitrogen-doped titanium dioxide nanoparticles (N-TiONps) developed by Chen *et al.* demonstrated unique advantages under UV light. 1 hour was sufficient for the complete degradation of PAT in simulated and natural fruit juices, and the reaction mechanism study showed that superoxide radicals ($\cdot O_2^-$) and hydroxyl radicals ($\cdot OH$) The reaction mechanism study showed that $\cdot O_2^-$ and $\cdot OH$ are the main reactive species, and combined with the density functional theory (DFT) calculation confirmed that ester group is the key site of radical attack, which provides theoretical support for the degradation pathway at molecular level.[169]

In the same period, in another study, La-ZnFeO@FeO@carbon magnetic composites prepared with Fe/Zn metal–organic framework (MOF) as precursor showed 97.35% degradation of PAT under UV light, and the improved performance was attributed to the charge separation efficiency promoted by La doping and the multilevel active interfaces constructed with multifaceted components, which was further

verified by electron spin resonance (ESR) analysis ·OH and $\cdot O_2^-$ dominant roles.[170]

In the optimization of photocatalytic material structure, TiO_2 nanotubes (TNTs) prepared by hydrothermal method combined with calcination showed unique advantages. Calcined at 450 °C, TNTs-450 can completely degrade 1000 μg L^{-1} PAT in simulated juice in 25 min with the high surface hydroxyl density of the amorphous structure, the mass transfer advantage of mesoporous nanotube structure, and the enhanced UV absorption, and the kinetic study shows that the degradation process is in accordance with the one-stage reaction model and Langmuir–Hinshelwood adsorption–surface reaction mechanism, which provided an efficient solution to the problem of PAT exceeding the standard in juice industry.[168]

The functionalized design of g-C_3N_4 matrix composites further expands the application scenarios. The g-C_3N_4-SH@KG aerogel prepared by glutaraldehyde cross-linking to introduce sulfhydryl groups (–SH) and immobilized with konjac glucomannan (KG) was constructed in a "dark adsorption–light regeneration" cyclic mode. The specific adsorption of PAT by sulfhydryl groups was rapidly accomplished in the dark environment, and the photocatalytic activity of g-C_3N_4 in the light achieved the regeneration of the adsorption sites, which was both highly efficient in removal and reuse.[41]

The g-C_3N_4 composites are also widely used in other applications. Ma *et al.* prepared a multifunctional magnetic g-C_3N_4/Fe_3O_4 nanocomposite (Fig. 7D), which exhibited a strong adsorption capacity for substances in complex matrices and realized a convenient magnetic separation from the sample solution.[160] According to the research results published by Shi and other scholars, when the cross-linking reaction between g-C_3N_4 and sodium alginate occurs, which leads to the formation of nanocomposite hydrogels, the thermal stability of the gel is greatly enhanced, and the mechanical properties are also significantly improved, which demonstrates a greater advantage in practical applications.[171] In contrast, Gahlot *et al.* showed that a significant enhancement of thermal stability could be achieved by adding 0.5 wt% graphene to PVA nanocomposites.[172] This phenomenon is attributed to the strong interfacial interactions between graphene and polymers, which are essential for enhancing the physical properties of hydrogels.[173] Notably, the composite system of g-C_3N_4 with hydrophilic polymers (*e.g.*, sodium alginate, polyvinyl alcohol) not only enhances the mechanical strength and thermal stability of the hydrogel through interfacial interactions, but its abundant functional groups also synergize with the photocatalytic active sites to form a multi-trapping, directed degradation network. Combining g-C_3N_4 with hydrophilic polymers can also significantly enhance the mechanical properties, thermal stability and adsorption capacity of hydrogels.[174] The successful application of this structural design strategy in dye decolorization and heavy metal removal further confirms its potential value in food toxin management.[175] Future research could focus on the development of visible light-responsive composites, the optimization of the fitness of interfering factors in real food matrices, and the in-depth analysis of the degradation pathway based on *in situ* characterization techniques, to promote the key leap of photocatalytic technology from the laboratory to industrial applications.

In addition to being used for PAT removal, graphite-phase carbon nitride-based materials have been widely used to treat other pollutants. Zinc-enriched g-C_3N_4 was prepared in the experiments of Chen *et al.* When the salinity increased from 0.1 wt% to 2.3 wt%, the removal efficiency of 2,4-DCP by the material slightly increased. This material exhibited exceptional efficiency in eliminating 2,4-DCP, achieving a removal rate exceeding 75.6%, this particular quantity was two times as large as what was observed in the case of pure g-C_3N_4 and g-C_3N_4 that had been treated with Co, Ag, Mo, and Bi. Once 0.1 g L^{-1} of g-C_3N_4 having a significant amount of zinc was introduced, the percentages by which 2,4-DCP, 2-chlorohydroquinone, chloroacetophenone, and 2-chloropropionic acid were removed reached the values of 99.3%, 99.8%, 98.2%, and 99.9% respectively.[176] Liu *et al.* succeeded in constructing Ag_3PO_4/Ag/g-C_3N_4 heterojunctions, which have a wide range of light absorption, *via* a hydrothermal method. Under visible light, Ag_3PO_4/Ag/g-C_3N_4-1.6 demonstrated a superior methyl orange removal rate (~90%) compared to Ag_3PO_4 or Ag/g-C_3N_4 alone. Its degradation rate of 0.04126 min^{-1} was 4.23 and 6.53 times higher than that of Ag_3PO_4/Ag and g-C_3N_4, respectively. The enhanced photocurrent intensity of Ag_3PO_4/Ag/g-C_3N_4 suggests improved the efficiency of separating the electron–hole pairs that are generated by photo-excitation, attributed to the material's heterojunction structure. Even after five cycles, the photocatalyst retained high activity. The exceptional performance under UV-visible light is linked to the effective carrier separation enabled by the Ag_3PO_4/Ag/g-C_3N_4 heterostructure.[177] In the research conducted by Mahmoudi and colleagues, g-C_3N_4/Fe_3O_4 nanocomposites were employed as catalysts through a straightforward hydrothermal approach. The influence of critical operational factors, including initial pH, catalyst dosage, contact duration, and initial oxytetracycline (OTC) concentration in aqueous solution, was examined under UV light. Optimal OTC removal efficiency (99.8%) was attained under neutral pH conditions (pH 7) with a catalyst loading of 0.7 g L^{-1} and an initial OTC concentration of 5 mg L^{-1}.[178]

4.2 Graphite-phase carbon nitride-based materials for energy storage applications

Renowned for its outstanding chemical and physical stability, environmental-friendliness, and non-pollution, g-C_3N_4 is a widely-acknowledged 2D semiconductor material. Due to its exceptional characteristics, g-C_3N_4 has found widespread use in various energy storage arrangements, encompassing lithium-ion, lithium-sulfur, sodium-ion, and potassium-ion accumulators, in addition to supercondensers.[179] Electrochemical energy storage systems are those that are designed to store energy through electrochemical processes. They include two main types of components. One type is batteries, which are devices that convert chemical energy into electrical energy and *vice versa*. The other type is supercapacitors (SCs), which store energy electrostatically and can charge and discharge much faster than batteries, have significantly impacted the field of

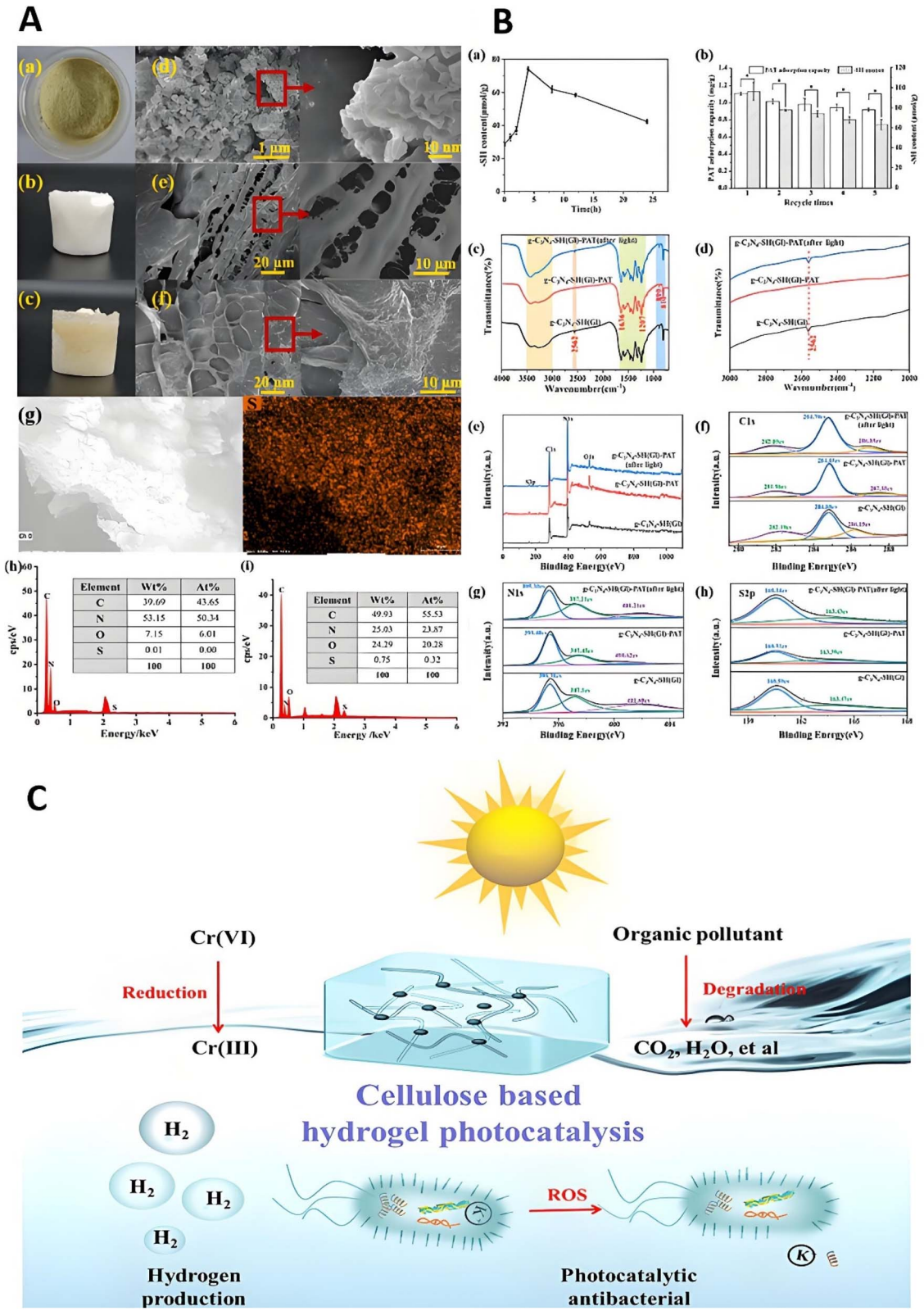

Fig. 9 Composite gel materials are used for PAT removal, as well as other applications. (A), (a) Photos of g-C_3N_4-SH(Gl), (b) a pure konjac aerogel sample, and (c) g-C_3N_4-SH (Gl)@KG-5 are presented. Scanning Electron Microscopy (SEM) pictures of (d) g-C_3N_4-SH(Gl), (e) the pure konjac aerogel, and (f) g-C_3N_4-SH (Gl)@KG-5 are shown at various magnifications. Moreover, (g) elemental mappings of sulfur (S) for g-C_3N_4-SH (Gl) @KG-5 using SEM-Energy-Dispersive X-ray (SEM-EDX) analysis are provided. Energy-Dispersive X-ray (EDX) spectra of (h) g-C_3N_4 and (i) g-C_3N_4-SH (Gl)@KG-5 are also included.[35] (B), (a) Variations in the duration of photocatalytic treatment and the concentration of –SH groups; (b) the reusability of g-C_3N_4-SH(Gl)@KG-5 for the adsorption of PAT in PCBs. (c and d) Fourier-Transform Infrared (FT-IR) spectral profiles of g-

energy applications (Fig. 8A). Hussain *et al.* demonstrated a new approach to fabricate g-C_3N_4 for supercapacitor devices using spinel oxide materials. They synthesized $MnFe_2O_4$, g-C_3N_4, and $MnFe_2O_4$@g-C_3N_4 nanocomposites through a hydrothermal method to study their electrochemical properties. The $MnFe_2O_4$@g-C_3N_4 nanohybrids showed a particular capacitance (Cs) of 1414 F g^{-1} at 1 A g^{-1} and excellent durability after the 5th, 5000th cycle, as determined from the Nyquist plot. The small charge transfer impedance (R_{ct} = 0.08 Ω) suggested that this material performs well in supercapacitor applications. In addition, they performed symmetric two-electrode tests on $MnFe_2O_4$@g-C_3N_4 nanohybrids possessing a Cs of 392.02 F g^{-1} at 1 A g^{-1}, this phenomenon can be ascribed to the robust interfacial interactions existing between $MnFe_2O_4$ and g-C_3N_4.[161] Wu *et al.* developed nitrogen-doped graphitic carbon nanosheets (NGCNs) through a straightforward reaction involving g-C_3N_4 and CaC_2. The resulting NGCN exhibits a elevated nitrogen content (3.98 at%), a substantial specific surface area (72.96 m^2 g^{-1}), and a high degree of graphitization (interlayer spacing of 0.335 nm). As an negative electrode material for lithium-ion batteries, NGCN demonstrates a promising reversible capacity of 475 mA h g^{-1} at 500 mA g^{-1}, maintaining 98.5% capacity retention after 1000 cycles. Additionally, it shows a respectable rate capability (238 mA h g^{-1} at 5000 mA g^{-1}). This investigation presents a plausible tactic to convert renewable carbon sources into nitrogen-incorporated graphitic carbon nanoplates with remarkable electrochemical characteristics.[180]

4.3 Graphite-phase carbon nitride-based materials for energy conversion applications

The rational development and sustainable preparation of g-C_3N_4-based materials enable their wide-ranging applications in energy conversion and storage fields. These applications cover various aspects, like photocatalytic H_2 release, photocatalytic O_2 release, photocatalytic total water decomposition, CO_2 photoreduction, electrocatalytic H_2 release, O_2 release, and O_2 reduction.[163] The photocatalytic fuel cell (PFC) system is a major innovation within the domain of energy transformation technology, which uses the potential of organic waste to generate electricity. A new method for simultaneous power generation and pollutant removal using a PFC system consisting of Bi_2O_3/TiO_2 heterojunction nanotubes modified with g-C_3N_4 as the photoanode material was presented By Zhao and colleagues. The g-C_3N_4/Bi_2O_3/TiO_2 (CBT) heterostructure has a large specific surface region, better visible photonic absorption and enhanced photogenerated charge-carrier segregation. In the case where tetracycline hydrochloride was employed as the pollutant that was specifically targeted, the ability of the CBT heterostructures to perform photocatalytic degradation was 3.2 times as great as the corresponding ability of pure TiO_2 nanotubes. In addition, the PFC system consisting of CBTs as photoanodes significantly improved the pollutant degradation and current output compared with those of the PFC system with pure TiO_2. This study presents a cost-effective method for organic waste treatment and simultaneous power generation.[164] In 2023, Sowmya and Vijaikanth introduced an economical modified electrode incorporating g-C_3N_4/chlorocobalt oxime composites, showcasing their electrocatalytic performance for hydrogen evolution reaction (HER) (Fig. 8B) and oxygen evolution reaction (OER) (Fig. 8C), alongside their energy storage potential. Hydrolysis experiments of the g-C_3N_4/ClCo(dpgH)$_2$ (pyridine-3,5-dicarboxylic acid) composite in 0.5 M KOH demonstrated sustained hydrogen and oxygen generation for up to 120 hours. The composite was characterized by a high level of hydrogen and oxygen release over a period of up to 120 h. The composite was then subjected to an electrocatalytic reaction (HER) and oxygen release (OER), which was characterized by a high level of hydrogen and oxygen. Supercapacitor application studies *via* cyclic voltammetry and charge/discharge studies revealed that the g-C_3N_4/ClCo(dpgH)$_2$ (isonicotinic acid) nanocomposite has a high specific capacity of 236 F g^{-1} at 0.5 A g^{-1}.[165]

The high dispersibility of g-C_3N_4 can make its separation from solutions challenging, often requiring time-consuming centrifugation. In contrast, Fe_3O_4 particles can be easily isolated using an external magnet. Thus, incorporating Fe_3O_4 onto the g-C_3N_4 surface presents a practical solution to address this issue effectively. In 2021, Ma *et al.* prepared a multifunctional magnetic g-C_3N_4/Fe_3O_4 nanocomposite material to be used as a modified QuEChERS adsorbent through ultra-high-performance liquid chromatography-tandem mass spectrometry (UPLC-MS/MS). This precise quantification method combines multiple methods. The g-C_3N_4/Fe_3O_4 composite not only strongly adsorbs substances on complex substrates but also achieves convenient magnetic separation from the sample solution.[160]

Fe_3O_4/ZIFs possess a large specific surface area and a hierarchical porous structure comprising micropores and mesopores, along with abundant π–π and Zn-N*x* groups. These characteristics render Fe_3O_4/ZIFs highly effective adsorbents, offering numerous adsorption sites and multifunctional groups that align with the analyte's chemical structure, leading to excellent adsorption performance. In 2023, a controlled magnetic adsorbent of Fe_3O_4/ZIFs was studied by Zhang *et al.* Through altering the proportion of Fe^{2+} to Zn^{2+}, the specific surface area of Fe_3O_4/ZIFs is tunable, thereby affecting performance. Research has revealed that for Fe_3O_4/ZIFs (1 : 8), the adsorption efficiency of the two precursor substances of AFB_1 (AVN, ST) is the highest, and this material has a certain degree of reusability.[159]

Many aspects of hydrogels, including a high water content, excellent biocompatibility and controllable network structure, have been obtained. Extremely extensive and in-depth

C_3N_4, g-C_3N_4-SH(Gl)-PAT, and g-C_3N_4-SH(Gl)-PAT subsequent to light exposure. (e) Overall XPS spectral scans of g-C_3N_4, g-C_3N_4-SH(Gl)-PAT, and g-C_3N_4-SH(Gl)-PAT following light exposure. High-resolution XPS spectral analyses of carbon (C) 1s (f), nitrogen (N) 1s (g), and sulfur (S) 2p (h) For g-C_3N_4, g-C_3N_4-SH(Gl)-PAT, and g-C_3N_4-SH(Gl)-PAT after being subjected to light.[35] (C) Hydrogel photocatalytic application.[146]

application. According to research results published by Shi and other scholars, when g-C_3N_4 reacts with sodium alginate and then forms a nanocomposite hydrogel, the thermal stability of the gel is greatly enhanced, and the mechanical properties are significantly improved. This approach has advantages in practical applications.[142] Research by Gahlot and associates demonstrated that within PVA nanocomposites, only 0.5 wt% graphene is required to achieve a significant increase in thermal stability.[143] This effect is due to the robust interfacial interaction between graphene and the polymer, playing a key role in enhancing the hydrogel's physical properties.[144] Considering the structural resemblance between g-C_3N_4 and graphene, we hypothesize that incorporating g-C_3N_4 with hydrophilic polymers can remarkably enhance the mechanical characteristics, thermal endurance, and adsorption capability of the hydrogel.[145] In addition, some researchers have grafted SH with visible light catalytic properties *via* glutaraldehyde cross-linking and immobilized it with KG in order to acquire a composite aerogel g-C_3N_4-SH (Gl)@KG-5 material, this material was employed for the elimination of PAT in juice (Fig. 9A and B).[35] Moreover, hydrogels are additionally employed for the removal of dyes and heavy-metal ions, antibacterial applications, and photocatalytic hydrogen generation, among other purposes (Fig. 9C).[146] These studies suggest that the removal efficiency of g-C_3N_4/GO/Fe_3O_4/ZIF-8 nanohydrogel composites for PAT is significantly greater than that of traditional methods.

Composite materials such as GO, Fe_3O_4 and ZIF-8 possess extensive application potential in the domains of food safety and environmental conservation. The composite material can be used to remove PAT and contaminate fruits and their products, as well as a variety of mycotoxins, such as deoxyfusarium enol (DON), AFB_1, zearalenone (ZEN), and ochratoxin A (OTA), to improve the safety of food; at the same time, it can also be used to treat wastewater, soil and other environmental pollutants containing mycotoxins to protect the ecological environment.

5 Conclusion and prospects

The g-C_3N_4-based materials show remarkable potential in the field of adsorption and photocatalytic synergistic removal of PAT due to their unique two-dimensional layered structure, visible-light-responsive properties and excellent chemical stability. It has been shown that its large specific surface area and abundant surface functional groups can realize efficient adsorption and enrichment of PAT through electrostatic interaction, hydrogen bonding and π–π stacking, while the photocatalytic process can gradually degrade PAT into harmless small molecules through the generation of reactive oxygen species (*e.g.*, ·OH and $\cdot O_2^-$) by stimulating electron–hole pairs. The synergistic effect of adsorption and photocatalysis not only improves the PAT removal efficiency, but also maintains the adsorption capacity of the material through dynamic equilibrium. Currently, this technology has been validated in food matrices such as fruit juice and fruit wine, and has shown promising applications in environmental treatment scenarios such as wastewater purification and soil remediation. However, the high complexity of photogenerated carriers, the lack of stability in complex environments, and the lack of a scale-up preparation process remain the core challenges limiting its practical application.

In recent years, emerging research trends have focused on exploring interdisciplinary means to optimize material properties and expand application boundaries. For example, heterostructure construction modulates carrier separation efficiency through energy band engineering, and Yang *et al.* achieved 100% removal rate of PAT through TiO_2/g-C_3N_4 heterojunction with significantly better synergistic effect than single component (Fig. 7D).[160] Multi-dimensional structural design can simultaneously enhance the adsorption capacity and photoresponsive activity, and the CN/GO/SA hydrogel microspheres developed by Sun *et al.* achieved up to 98.4% removal of AFB_1 from peanut oil with excellent cycling stability.[157] In addition, the rise of intelligent composites provides new ideas for PAT control, such as light-responsive hydrogels for targeted adsorption and degradation of pollutants through *in situ* polymerization.[41] These advances indicate that the performance boundaries of g-C_3N_4-based materials are being broken through the deep integration of materials science and environmental engineering.

Future studies need to deepen the exploration in the following directions: first, the refinement of mechanistic studies needs to combine *in situ* characterization techniques with theoretical calculations to clarify the PAT degradation pathway and the toxicity evolution of intermediates. Liu *et al.* revealed the promotion of carrier migration by nitrogen vacancies in P-doped g-C_3N_4 through DFT,[179] and this kind of study can provide atomic-level guidance. Second, the development of functional composite systems needs to focus on multitechnology synergies, combining g-C_3N_4 with magnetic materials to simplify the recycling process by using magnetic separation technology, or coupling with biodegradation technology to achieve the harmless transformation of pollutants. Recently, Zhang *et al.* designed Fe_3O_4/ZIFs magnetic adsorbents to achieve efficient capture of mycotoxin precursors by modulating the pore structure,[159] a strategy that can be extended to the field of PAT governance. In addition, the suitability for practical application scenarios needs to be focused on, such as the development of flexible photocatalytic membranes (*e.g.*, electrostatically spun g-C_3N_4/MoS_2 membranes) to suit the continuous operation in food processing.[158]

At the EHS level, the long-term ecological risks of g-C_3N_4-based materials need to be systematically assessed. For example, the potential bioaccumulation of nanoparticles and their effects on non-target organisms have not been clarified.[174] In addition, the synergistic removal mechanism of multifunctional composites for composite pollutants still needs to be deeply analyzed. Optimization of the preparation process through life cycle analysis and green chemistry principles will be the key to achieve sustainable development of the materials.[180]

In conclusion, g-C_3N_4-based materials have demonstrated the potential to transition from laboratory research to industrialization in PAT pollution control. Through interdisciplinary

innovation and engineering exploration, the future is expected to build an efficient, green and economical technology system for PAT management, providing more competitive solutions for food safety and environmental protection.

Data availability

No primary research results, software or code have been included and no new data were generated or analysed as part of this review.

Conflicts of interest

The authors declare no conflict of interest.

Acknowledgements

This work was supported by the Natural Science Foundation Project of Hubei Province (2022CFB533) and the Scientific Research Plan of Education Department of Hubei Province (D20222702), and the Natural Science Project of Xiaogan City (XGKJ2024030002).

References

1 I. Chalmers and M. Clarke, *Int. J. Epidemiol.*, 2004, **33**, 253–260.
2 G. L. Ngolong Ngea, Q. Yang, R. Castoria, X. Zhang, M. N. Routledge and H. Zhang, *Compr. Rev. Food Sci. Food Saf.*, 2020, **19**, 2447–2472.
3 L. Zhong, J. Carere, Z. Lu, F. Lu and T. Zhou, *Toxins*, 2018, **10**, 475.
4 N. De Clercq, G. Vlaemynck, E. Van Pamel, D. Colman, M. Heyndrickx, F. Van Hove, B. De Meulenaer, F. Devlieghere and E. Van Coillie, *World Mycotoxin J.*, 2016, **9**, 379–388.
5 S. Barad, E. Sionov and D. Prusky, *Fungal Biol. Rev.*, 2016, **30**, 24–32.
6 H. Dai, Y. Huang and H. Huang, *Carbohydr. Polym.*, 2018, **185**, 1–11.
7 J. Niu, B. Ma, J. Shen, H. Zhu, Y. Lu, Z. Lu, F. Lu and P. Zhu, *Food Microbiol.*, 2025, **126**, 104676.
8 S. Ramalingam, A. Bahuguna and M. Kim, *Trends Food Sci. Technol.*, 2019, **83**, 99–113.
9 X. Zheng, W. Wei, W. Zhou, H. Li, S. Rao, L. Gao and Z. Yang, *Food Res. Int.*, 2021, **140**, 110034.
10 I. Saleh and I. Goktepe, *Food Chem. Toxicol.*, 2019, **129**, 301–311.
11 P. Udomkun, A. N. Wiredu, M. Nagle, J. Müller, B. Vanlauwe and R. Bandyopadhyay, *Food Control*, 2017, **76**, 127–138.
12 S. K. Pankaj, H. Shi and K. M. Keener, *Trends Food Sci. Technol.*, 2018, **71**, 73–83.
13 J. Wan, B. Chen and J. Rao, *Compr. Rev. Food Sci. Food Saf.*, 2020, **19**, 928–953.
14 R. Khan, F. Anwar and F. M. Ghazali, *Heliyon*, 2024, **10**, e28361.
15 E. Kroke, M. Schwarz, E. Horath-Bordon, P. Kroll, B. Noll and A. D. Norman, *New J. Chem.*, 2002, **26**, 508–512.
16 Q. Hao, G. Jia, W. Wei, A. Vinu, Y. Wang, H. Arandiyan and B.-J. Ni, *Nano Res.*, 2020, **13**, 18–37.
17 G. Liao, Y. Gong, L. Zhang, H. Gao, G.-J. Yang and B. Fang, *Energy Environ. Sci.*, 2019, **12**, 2080–2147.
18 M. Ismael, *J. Alloys Compd.*, 2020, **846**, 156446.
19 S. Yang, Y. Gong, J. Zhang, L. Zhan, L. Ma, Z. Fang, R. Vajtai, X. Wang and P. M. Ajayan, *Adv. Mater.*, 2013, **25**, 2452–2456.
20 F. Cheng, H. Wang and X. Dong, *Chem. Commun.*, 2015, **51**, 7176–7179.
21 P. Niu, L. Zhang, G. Liu and H. Cheng, *Adv. Funct. Mater.*, 2012, **22**, 4763–4770.
22 S. Yin, J. Han, T. Zhou and R. Xu, *Catal. Sci. Technol.*, 2015, **5**, 5048–5061.
23 S. K. Selvam, R. A. Kumar, N. Balasubramanian, P. S. Kumar, A. Muthukrishnaraj, S. S. Kalaivani, R. Vinayagam, R. S. Azarudeen, M. A. R. Ahamed, A. Harikrishnan, S. Josephine, G. A and G. Rangasamy, *Desalin. Water Treat.*, 2024, **318**, 100385.
24 E. Baur and A. Perret, *Helv. Chim. Acta*, 1924, **7**, 910–915.
25 A. Fujishima and K. Honda, *Nature*, 1972, **238**, 37–38.
26 J. H. Carey, J. Lawrence and H. M. Tosine, *Bull. Environ. Contam. Toxicol.*, 1976, **16**, 697–701.
27 Y. Shi, Q. Zhao, J. Li, G. Gao and J. Zhi, *Appl. Catal., B*, 2022, **308**, 121216.
28 O. S. Keen, S. Baik, K. G. Linden, D. S. Aga and N. G. Love, *Environ. Sci. Technol.*, 2012, **46**, 6222–6227.
29 J. K. Glenn and J. Goldman, *Am. J. Public Health*, 1976, **66**, 64–66.
30 E. Haque, J. W. Jun, S. N. Talapaneni, A. Vinu and S. H. Jhung, *J. Mater. Chem.*, 2010, **20**, 10801.
31 Y. Cui, Z. Ding, X. Fu and X. Wang, *Angew. Chem.*, 2012, **124**, 11984–11988.
32 Q. Liao, W. Pan, D. Zou, R. Shen, G. Sheng, X. Li, Y. Zhu, L. Dong, A. M. Asiri, K. A. Alamry and W. Linghu, *J. Mol. Liq.*, 2018, **261**, 32–40.
33 W. Wang, Q. He, Y. Yi, Y. Xiao, X. Xiao, H. Yang and X. Dong, *J. Cleaner Prod.*, 2023, **415**, 137818.
34 B. Zhu, P. Xia, W. Ho and J. Yu, *Appl. Surf. Sci.*, 2015, **344**, 188–195.
35 J. Wang, D. Yue, D. Cui, L. Zhang and X. Dong, *Environ. Sci. Technol.*, 2021, **55**, 7910–7919.
36 H. Wu, W. Zhang, H. Zhang, Y. Pan, X. Yang, Z. Pan, X. Yu and D. Wang, *Colloids Surf., A*, 2020, **607**, 125517.
37 X. Li, J. Yu, J. Low, Y. Fang, J. Xiao and X. Chen, *J. Mater. Chem. A*, 2015, **3**, 2485–2534.
38 Y. Gong, M. Li and Y. Wang, *ChemSusChem*, 2015, **8**, 931–946.
39 Y. Jun, E. Z. Lee, X. Wang, W. H. Hong, G. D. Stucky and A. Thomas, *Adv. Funct. Mater.*, 2013, **23**, 3661–3667.
40 P. A. Poole-Wilson and G. A. Langer, *Am. J. Physiol.*, 1975, **229**, 570–581.
41 Y. Qiu, J. Yan, X. Liu, Y. Pang, Y. Ding and F. Lyu, *Food Chem.*, 2024, **451**, 139421.

42 R. A. M. Magzoub, A. A. A. Yassin, A. M. Abdel-Rahim, E. A. Gubartallah, M. Miskam, B. Saad and S. Sabar, *Food Control*, 2019, **95**, 206–214.
43 H. Zhang, P. Wu, J. He, W. Jiang and C. Liu, *J. Environ. Chem. Eng.*, 2021, **9**, 106430.
44 D. Sun, J. Mao, L. Cheng, X. Yang, H. Li, L. Zhang, W. Zhang, Q. Zhang and P. Li, *Chem. Eng. J.*, 2021, **418**, 129417.
45 C. Hu, C. Huang and B. Peng, *Food Chem.*, 2023, **426**, 136592.
46 X. Yang, J. Pan, J. Hu, S. Zhao and K. Cheng, *Chem. Eng. J.*, 2023, **467**, 143381.
47 Q. Sun, Z. Li, J. Li, N. Liu, M. Zhang and T. Le, *J. Alloys Compd.*, 2023, **955**, 170234.
48 R. Dhodapkar, N. N. Rao, S. P. Pande, T. Nandy and S. Devotta, *React. Funct. Polym.*, 2007, **67**, 540–548.
49 Y. Xing, D. Liu and L.-P. Zhang, *Desalination*, 2010, **259**, 187–191.
50 T. Kahn, J. Bosch, M. F. Levitt and M. H. Goldstein, *Am. J. Physiol.*, 1975, **229**, 746–753.
51 S. Y. Kim, J. Oh, S. Park, Y. Shim and S. Park, *Chem.–Eur. J.*, 2016, **22**, 5142–5145.
52 J. Liu, W. Li, L. Duan, X. Li, L. Ji, Z. Geng, K. Huang, L. Lu, L. Zhou, Z. Liu, W. Chen, L. Liu, S. Feng and Y. Zhang, *Nano Lett.*, 2015, **15**, 5137–5142.
53 H.-J. Li, B.-W. Sun, L. Sui, D.-J. Qian and M. Chen, *Phys. Chem. Chem. Phys.*, 2015, **17**, 3309–3315.
54 J.-S. Chen, T.-C. Lo, Y.-C. Hsieh, C.-H. Chen, M. Lin, H.-Y. Lin, M.-W. Hung, H.-R. Wu and S.-Y. Luo, *ACS Omega*, 2023, **8**, 8885–8893.
55 A. Sudha, I. Manimehan, B. Sundaresan, R. Arivuselvi, S. Manimaran, M. Ayyanar, P. Gangapriya and K. Ravichandran, *Appl. Phys. A*, 2025, **131**, 393.
56 G. Huang, S. Huo, J. Ren, W. Chen, H. Yang, S. Xiao, T. Wang, H. Peng and P. Song, *Appl. Mater. Today*, 2024, **38**, 102191.
57 L. Nguyen Thi, N. N. Tri, L. N. Tan, N. M. Vuong, T.-L. Thi Le, D. Thi To Nu, L. T. Nguyen, D. T. Khan, L. V. T. Son, T. N. Dat, V. T. Nguyen, Q. T. H. Ta, V. A. Tran, T. T. Trang Phan and V. Vo, *J. Alloys Compd.*, 2025, **1018**, 179245.
58 K. I. John, T. B. Issa, G. Ho, A. N. Nikoloski and D. Li, *Water Cycle*, 2025, **6**, 151–175.
59 É. W. A. Almeida, C. M. C. Dazon, M. D. V. R. Rodriguez, T. M. Nobre, M. C. Pereira and D. S. Monteiro, *ACS Omega*, 2025, **10**, 17024–17032.
60 M. Hosseini, M. Ghanbari, M. A. Mahdi, M. H. Almaamori, Z. A. A. Alhassan and M. Salavati-Niasari, *Appl. Water Sci.*, 2025, **15**, 41.
61 J. Chen, J. Lu, R. Lang, C. Wang, S. Bao, Y. Li, K. Li and M. Fan, *Green Energy Environ.*, 2025, **10**, 1348–1358.
62 S. Marouch, G. Sarp, M. Soylak and E. Yilmaz, *ACS Omega*, 2025, **10**, 11961–11971.
63 V. Jeyalakshmi, S. Wu, S. Qin, X. Zhou, B. B. Sarma, D. E. Doronkin, J. Kolařík, M. Šoóš and P. Schmuki, *Chem. Sci.*, 2025, **16**, 4788–4795.
64 N. Mamba, T. A. Makhetha, B. S. Mbuli and S. P. Malinga, *Inorg. Chem. Commun.*, 2025, **176**, 114215.
65 N. Alebachew, T. B. Demissie, H. C. A. Murthy, B. A. Gonfa, K. G. Von Eschwege, E. Coetsee, E. H. G. Langner, Jayadev and B. H. Doreswamy, *RSC Adv.*, 2025, **15**, 6441–6456.
66 M. Yaqoubi, M. Ghanbari, R. W. Maya, H. A. Jasim and M. Salavati-Niasari, *Results Eng.*, 2025, **25**, 104037.
67 L. Santamaría, S. A. Korili, A. Gil, J. M. López-de-Luzuriaga and M. Monge, *Appl. Surf. Sci.*, 2024, **673**, 160906.
68 Y. Qiu, J. Yan, X. Liu, Y. Pang, Y. Ding and F. Lyu, *Food Chem.*, 2024, **451**, 139421.
69 S. Sun, J. Yang, M. Ku, W. Zhang, Y. Xie and R. Zhao, *SSRN*, 2024, **42**, 679–692.
70 X. Ruan, L. Wang, D. Liang and Y. Shi, *Langmuir*, 2023, **39**, 3371–3379.
71 Y. Yang, Z. Liu, R. Jiang, R. Li and X. Li, *J. Alloys Compd.*, 2019, **811**, 151991.
72 J. Zhang, M. Zhang, R. Sun and X. Wang, *Angew. Chem.*, 2012, **124**, 10292–10296.
73 X. Wang, K. Maeda, X. Chen, K. Takanabe, K. Domen, Y. Hou, X. Fu and M. Antonietti, *J. Am. Chem. Soc.*, 2009, **131**, 1680–1681.
74 M. Wang, J. Cheng, X. Wang, X. Hong, J. Fan and H. Yu, *Chin. J. Catal.*, 2021, **42**, 37–45.
75 Y. Xu, H. Xu, J. Yan, H. Li, L. Huang, J. Xia, S. Yin and H. Shu, *Colloids Surf., A*, 2013, **436**, 474–483.
76 J. Zhang, G. Zhang, X. Chen, S. Lin, L. Möhlmann, G. Dołęga, G. Lipner, M. Antonietti, S. Blechert and X. Wang, *Angew. Chem.*, 2012, **124**, 3237–3241.
77 J. Zhang, X. Chen, K. Takanabe, K. Maeda, K. Domen, J. D. Epping, X. Fu, M. Antonietti and X. Wang, *Angew. Chem.*, 2010, **122**, 451–454.
78 H. Li, C. Liu, A. Saini, Y. Wang, H. Jiang, T. Yang, L. Chen, C. Pan and H. Shen, *J. Power Sources*, 2019, **438**, 226974.
79 Y. Wang, H. Wang, J.-S. He and X. Feng, *Nat. Commun.*, 2017, **8**, 15972.
80 S. Cao, J. Low, J. Yu and M. Jaroniec, *Adv. Mater.*, 2015, **27**, 2150–2176.
81 Z. Cai, Y. Zhou, S. Ma, S. Li, H. Yang, S. Zhao, X. Zhong and W. Wu, *J. Photochem. Photobiol., A*, 2017, **348**, 168–178.
82 B. Modak and S. K. Ghosh, *J. Phys. Chem. C*, 2016, **120**, 6920–6929.
83 J. Tian, Q. Liu, A. M. Asiri, A. H. Qusti, A. O. Al-Youbi and X. Sun, *Nanoscale*, 2013, **5**, 11604.
84 Z. Li, C. Kong and G. Lu, *J. Phys. Chem. C*, 2016, **120**, 56–63.
85 B. Yue, Q. Li, H. Iwai, T. Kako and J. Ye, *Sci. Technol. Adv. Mater.*, 2011, **12**, 034401.
86 S. Hu, R. Jin, G. Lu, D. Liu and J. Gui, *RSC Adv.*, 2014, **4**, 24863.
87 L. Cao, R. Wang and D. Wang, *Mater. Lett.*, 2015, **149**, 50–53.
88 J. Liu, *J. Alloys Compd.*, 2016, **672**, 271–276.
89 J. Li, B. Shen, Z. Hong, B. Lin, B. Gao and Y. Chen, *Chem. Commun.*, 2012, **48**, 12017.
90 G. Dong, K. Zhao and L. Zhang, *Chem. Commun.*, 2012, **48**, 6178.
91 X. Li, J. Yu and M. Jaroniec, *Chem. Soc. Rev.*, 2016, **45**, 2603–2636.
92 J. Xu, Y. Wang and Y. Zhu, *Langmuir*, 2013, **29**, 10566–10572.

93 Y. Zhang, J. Liu, G. Wu and W. Chen, *Nanoscale*, 2012, **4**, 5300.
94 J. Zhang, F. Guo and X. Wang, *Adv. Funct. Mater.*, 2013, **23**, 3008–3014.
95 X.-H. Li, J. Zhang, X. Chen, A. Fischer, A. Thomas, M. Antonietti and X. Wang, *Chem. Mater.*, 2011, **23**, 4344–4348.
96 Y. Cui, J. Huang, X. Fu and X. Wang, *Catal. Sci. Technol.*, 2012, **2**, 1396.
97 X.-H. Li, X. Wang and M. Antonietti, *Chem. Sci.*, 2012, **3**, 2170.
98 X. Chen, C. Li, M. Grätzel, R. Kostecki and S. S. Mao, *Chem. Soc. Rev.*, 2012, **41**, 7909.
99 J. Ding, Q. Liu, Z. Zhang, X. Liu, J. Zhao, S. Cheng, B. Zong and W.-L. Dai, *Appl. Catal., B*, 2015, **165**, 511–518.
100 X. Wang, G. Sun, N. Li and P. Chen, *Chem. Soc. Rev.*, 2016, **45**, 2239–2262.
101 Y. Zhao, F. Zhao, X. Wang, C. Xu, Z. Zhang, G. Shi and L. Qu, *Angew. Chem., Int. Ed.*, 2014, **53**, 13934–13939.
102 J. Liu, H. Wang and M. Antonietti, *Chem. Soc. Rev.*, 2016, **45**, 2308–2326.
103 W. Wang, J. C. Yu, Z. Shen, D. K. L. Chan and T. Gu, *Chem. Commun.*, 2014, **50**, 10148–10150.
104 C. Hu, R. Chen and N. Zheng, *Adv. Mater.*, 2021, **33**, 2006159.
105 Y. Lu, Y. Wang and J. Zhang, *J. Phys. D: Appl. Phys.*, 2021, **54**, 313002.
106 G. Gardos and J. O. Cole, *Am. J. Psychiatry*, 1976, **133**, 32–36.
107 Z. Cao, J. Su, Y. Li, J. Li, Z. Wang, M. Li, B. Fan, G. Shao, H. Wang, H. Xu, R. Zhang and H. Lu, *J. Alloys Compd.*, 2021, **889**, 161771.
108 W. Wang, R. Yang, T. Li, S. Komarneni and B. Liu, *Composites, Part B*, 2021, **205**, 108512.
109 Z. Zhang, Q. Qian, B. Li and K. J. Chen, *ACS Appl. Mater. Interfaces*, 2018, **10**, 17419–17426.
110 J. H. Bombile, M. J. Janik and S. T. Milner, *Phys. Chem. Chem. Phys.*, 2019, **21**, 11999–12011.
111 W. Li, Y. Bai, C. Liu, Z. Yang, X. Feng, X. Lu, N. K. Van Der Laak and K.-Y. Chan, *Environ. Sci. Technol.*, 2009, **43**, 5423–5428.
112 Y. Sun, B. Sun, J. He and C. Wang, *InfoMat*, 2019, **1**, 496–524.
113 Q. Hua, X. Zhou, B. Zhang, M. Wang, J. Liu, Y. Wang and L. Jiang, *ACS Sustainable Chem. Eng.*, 2020, **8**, 2919–2930.
114 Q. Wang, Q. Gao, A. M. Al-Enizi, A. Nafady and S. Ma, *Inorg. Chem. Front.*, 2020, **7**, 300–339.
115 J. R. McKee, S. Hietala, J. Seitsonen, J. Laine, E. Kontturi and O. Ikkala, *ACS Macro Lett.*, 2014, **3**, 266–270.
116 X. Zhang, L. Xu, S. Wei, M. Zhai and J. Li, *J. Biomed. Mater. Res., Part A*, 2013, **101**, 2191–2201.
117 A. Saarai, T. Sedlacek, V. Kasparkova, T. Kitano and P. Saha, *J. Appl. Polym. Sci.*, 2012, **126**(S1), E79–E88.
118 J. Shin, J. S. Lee, C. Lee, H. Park, K. Yang, Y. Jin, J. H. Ryu, K. S. Hong, S. Moon, H. Chung, H. S. Yang, S. H. Um, J. Oh, D. Kim, H. Lee and S. Cho, *Adv. Funct. Mater.*, 2015, **25**, 3814–3824.
119 M. He and C. Chu, *J. Appl. Polym. Sci.*, 2013, **130**, 3736–3745.
120 P. V. O. Toledo, D. P. C. Limeira, N. C. Siqueira and D. F. S. Petri, *Cellulose*, 2019, **26**, 597–615.
121 J. Ma, Y. Xu, B. Fan and B. Liang, *Eur. Polym. J.*, 2007, **43**, 2221–2228.
122 Z. Tong, D. Yang, J. Shi, Y. Nan, Y. Sun and Z. Jiang, *ACS Appl. Mater. Interfaces*, 2015, **7**, 25693–25701.
123 Q. Han, Z. Cheng, J. Gao, Y. Zhao, Z. Zhang, L. Dai and L. Qu, *Adv. Funct. Mater.*, 2017, **27**, 1606352.
124 N. S. V. Capanema, A. A. P. Mansur, H. S. Mansur, A. C. De Jesus, S. M. Carvalho, P. Chagas and L. C. De Oliveira, *Environ. Technol.*, 2018, **39**, 2856–2872.
125 Y. S. Zhang and A. Khademhosseini, *Science*, 2017, **356**, eaaf3627.
126 D. Yang, *Chem. Mater.*, 2022, **34**, 1987–1989.
127 T.-C. Ho, C.-C. Chang, H.-P. Chan, T.-W. Chung, C.-W. Shu, K.-P. Chuang, T.-H. Duh, M.-H. Yang and Y.-C. Tyan, *Molecules*, 2022, **27**, 2902.
128 F. M. Croisfelt, L. L. Tundisi, J. A. Ataide, E. Silveira, E. B. Tambourgi, A. F. Jozala, E. M. B. Souto and P. G. Mazzola, *J. Mater. Sci.*, 2019, **54**, 10963–10983.
129 P. Mohammadzadeh Pakdel and S. J. Peighambardoust, *Carbohydr. Polym.*, 2018, **201**, 264–279.
130 T. K. Giri, A. Thakur, A. Alexander, Ajazuddin, H. Badwaik and D. K. Tripathi, *Acta Pharm. Sin. B*, 2012, **2**, 439–449.
131 Q. Tang, J. Lin and J. Wu, *J. Appl. Polym. Sci.*, 2008, **108**, 1490–1495.
132 J. W. Yu, J. Jung, Y.-M. Choi, J. H. Choi, J. Yu, J. K. Lee, N.-H. You and M. Goh, *Polym. Chem.*, 2016, **7**, 36–43.
133 H. Kasap, R. Godin, C. Jeay-Bizot, D. S. Achilleos, X. Fang, J. R. Durrant and E. Reisner, *ACS Catal.*, 2018, **8**, 6914–6926.
134 H. Xie, S. Tang, D. Li, S. Vongehr and X. Meng, *ChemSusChem*, 2017, **10**, 2301–2308.
135 V. Van Tran, D. Park and Y.-C. Lee, *Environ. Sci. Pollut. Res.*, 2018, **25**, 24569–24599.
136 F.-L. Mi, H.-W. Sung and S.-S. Shyu, *Carbohydr. Polym.*, 2002, **48**, 61–72.
137 S. S. Silva, A. Motta, M. T. Rodrigues, A. F. M. Pinheiro, M. E. Gomes, J. F. Mano, R. L. Reis and C. Migliaresi, *Biomacromolecules*, 2008, **9**, 2764–2774.
138 B.-L. Guo and Q.-Y. Gao, *Carbohydr. Res.*, 2007, **342**, 2416–2422.
139 M. V. Risbud and R. R. Bhond, *Drug Delivery*, 2000, **7**, 69–75.
140 S. Sajeesh and C. P. Sharma, *Drug Delivery*, 2011, **18**, 227–235.
141 T. Buranachai, N. Praphairaksit and N. Muangsin, *AAPS PharmSciTech*, 2010, **11**, 1128–1137.
142 W.-C. Lin, D.-G. Yu and M.-C. Yang, *Colloids Surf., B*, 2005, **44**, 143–151.
143 A. P. Rokhade, N. B. Shelke, S. A. Patil and T. M. Aminabhavi, *J. Microencapsulation*, 2007, **24**, 274–288.
144 Y. Chen and H. Tan, *Carbohydr. Res.*, 2006, **341**, 887–896.
145 J. You, F.-Q. Hu, Y.-Z. Du and H. Yuan, *Biomacromolecules*, 2007, **8**, 2450–2456.
146 P. Marcasuzaa, S. Reynaud, F. Ehrenfeld, A. Khoukh and J. Desbrieres, *Biomacromolecules*, 2010, **11**, 1684–1691.
147 I. M. El-Sherbiny, *Carbohydr. Polym.*, 2010, **80**, 1125–1136.

148 H. Cai, Z. P. Zhang, P. Chuan Sun, B. Lin He and X. Xia Zhu, *Radiat. Phys. Chem.*, 2005, **74**, 26–30.
149 I. M. El-Sherbiny and H. D. C. Smyth, *Carbohydr. Res.*, 2010, **345**, 2004–2012.
150 J. H. Hamman, *Mar. Drugs*, 2010, **8**, 1305–1322.
151 J. Zarate, L. Virdis, G. Orive, M. Igartua, R. M. Hernández and J. L. Pedraz, *J. Microencapsulation*, 2011, **28**, 614–620.
152 X. Wang, Y. Liang, W. An, J. Hu, Y. Zhu and W. Cui, *Appl. Catal., B*, 2017, **219**, 53–62.
153 J. Chen, X. Shi, L. Ren and Y. Wang, *Carbon*, 2017, **111**, 18–27.
154 D. Chen, J. Yang, Y. Zhu, Y. Zhang and Y. Zhu, *Appl. Catal., B*, 2018, **233**, 202–212.
155 L. Tang, C. Jia, Y. Xue, L. Li, A. Wang, G. Xu, N. Liu and M. Wu, *Appl. Catal., B*, 2017, **219**, 241–248.
156 X. Wu, S. Li, B. Wang, J. Liu and M. Yu, *Microporous Mesoporous Mater.*, 2017, **240**, 216–226.
157 S. Sun, J. Yang, Y. Liu, Y. Xie and F. Mwabulili, *Food Chem.*, 2023, **417**, 135964.
158 R. Song, L. Yao, C. Sun, D. Yu, H. Lin, G. Li, Z. Lian, S. Zhuang and D. Zhang, *Toxins*, 2023, **15**, 133.
159 Y. Zhang, Y. Man, J. Li, Y. Sun, X. Jiang, L. He and S. Zhang, *Talanta*, 2023, **259**, 124534.
160 S. Ma, L. G. Pan, T. You and K. Wang, *J. Agric. Food Chem.*, 2021, **69**, 4874–4882.
161 M. Hussain, A. M. Idris, J. Fatima, S. Chandra and A. Kumar, *J. Mater. Sci. Eng. B*, 2025, **313**, 117937.
162 Z. Wu, Z. Wang and X. Jin, *J. Energy Storage*, 2023, **72**, 108604.
163 O. Iqbal, H. Ali, N. Li, A. I. Al-Sulami, K. F Alshammari, H. S. M. Abd-Rabboh, Y. Al-Hadeethi, I. U. Din, A. I. Alharthi, R. Altamimi, A. Zada, Z. Wang, A. Hayat and M. Zahid Ansari, *Mater. Today Phys.*, 2023, **34**, 101080.
164 S.-Z. Zhao, R.-D. Shi, G.-T. Xiang, Y.-D. Hu and J.-J. Chen, *Fuel*, 2025, **386**, 134306.
165 S. Sowmya and V. Vijaikanth, *ACS Omega*, 2023, **8**, 32940–32954.
166 P. Chaluvachar, Y. N. Sudhakar, G. T. Mahesha, V. G. Nair, N. Desai and D. K. Pai, *J. Energy Chem.*, 2025, **103**, 498–524.
167 J. Yang, D. Liu, X. Song, Y. Zhao, Y. Wang, L. Rao, L. Fu, Z. Wang, X. Yang, Y. Li and Y. Liu, *Gels*, 2022, **8**, 270.
168 S. Sun, J. Yang, M. Ku, W. Zhang, Y. Xie and R. Zhao, *Food Addit. Contam.,:Part A*, 2024, **42**, 679–692.
169 D. Jeon, J. Park, C. Shin, H. Kim, J.-W. Jang, D. W. Lee and J. Ryu, *Sci. Adv.*, 2020, **6**, eaaz3944.
170 X. Yang, J. Pan, J. Hu, S. Zhao and K. Cheng, *Chem. Eng. J.*, 2023, **467**, 143381.
171 Y. Shi, S. Jiang, K. Zhou, C. Bao, B. Yu, X. Qian, B. Wang, N. Hong, P. Wen, Z. Gui, Y. Hu and R. K. K. Yuen, *ACS Appl. Mater. Interfaces*, 2014, **6**, 429–437.
172 S. Gahlot, V. Kulshrestha, G. Agarwal and P. K. Jha, *Macromol. Symp.*, 2015, **357**, 173–177.
173 H. Zhang, L. Zhao, F. Geng, L.-H. Guo, B. Wan and Y. Yang, *Appl. Catal., B*, 2016, **180**, 656–662.
174 Y. Zheng, L. Lin, B. Wang and X. Wang, *Angew. Chem.*, 2015, **127**, 13060–13077.
175 J. Yang, D. Liu, X. Song, Y. Zhao, Y. Wang, L. Rao, L. Fu, Z. Wang, X. Yang, Y. Li and Y. Liu, *Gels*, 2022, **8**, 270.
176 H. Chen, Y. Wang, S. Zhu, X. Wang, J. Liu, L. Wang, W. Fan and Y. Yu, *Water*, 2024, **16**, 2756.
177 Q. Liu, Y. Meng, Q. Liu, M. Xu, Y. Hu and S. Chen, *Molecules*, 2023, **28**, 6082.
178 K. Mahmoudi, M. Farzadkia, R. Rezaei Kalantary, H. R. Sobhi, M. Yeganeh and A. Esrafili, *Heliyon*, 2024, **10**, e30604.
179 X. Yang, J. Peng, L. Zhao, H. Zhang, J. Li, P. Yu, Y. Fan, J. Wang, H. Liu and S. Dou, *Carbon Energy*, 2024, **6**, e490.
180 Z. Wu, Z. Wang and X. Jin, *J. Energy Storage*, 2023, **72**, 108604.